

# INORGANIC CHEMISTRY

# FRONTIERS

RESEARCH ARTICLE

[View Article Online](#)  
[View Journal](#) | [View Issue](#)



Cite this: *Inorg. Chem. Front.*, 2023, **10**, 1999

## Magnetic and relaxation properties of vanadium(IV) complexes: an integrated $^1\text{H}$ relaxometric, EPR and computational study<sup>†</sup>

Valeria Lagostina,<sup>a</sup> Fabio Carniato,<sup>ID, b</sup> David Esteban-Gómez,<sup>ID, c</sup> Carlos Platas-Iglesias,<sup>ID, \*c</sup> Mario Chiesa<sup>ID, \*a</sup> and Mauro Botta<sup>ID, \*b</sup>

We report a detailed study of the magnetic and relaxation properties of a series of oxovanadium(IV) complexes comprising the aqua ion  $[\text{VO}(\text{H}_2\text{O})_5]^{2+}$  and  $[\text{VO}(\text{ox})_2]^{2-}$  (ox = oxalate),  $[\text{VO}(\text{nta})]^-$  (nta = nitrilotriacetate),  $[\text{VO}(\text{dtpa})]^{3-}$  (dtpa = diethylenetriaminepentaacetate) and  $[\text{VO}(\text{acac})_2]$  (acac = acetylacetone) in solution. The complexes were characterized using continuous wave (X-band) and pulsed (Q-band) EPR measurements and  $^1\text{H}$  nuclear magnetic relaxation dispersion (NMRD) studies in the 0.01–120 MHz  $^1\text{H}$  Larmor frequency range. The  $^{51}\text{V}$  A-tensor parameters obtained from the analysis of EPR spectra are in good agreement with those obtained using theoretical calculations at the DFT and coupled-cluster levels (DLPNO-CCSD), while g-tensors were obtained with CASSCF/NEVPT2 calculations. EPR measurements reveal significant differences in the electronic  $T_1^e$  and  $T_m^e$  relaxation times, with  $[\text{VO}(\text{acac})_2]$  showing a markedly different behaviour due to the *trans* coordination geometry. The NMRD profiles measured at different temperatures have contributions from both the outer- and inner-sphere mechanisms, with the latter showing contributions from the dipolar and scalar mechanisms. The rotational correlation times ( $\tau_R$ ) obtained from the fitting of NMRD and EPR data are in good mutual agreement. The scalar mechanism depends on the hyperfine coupling constants of the coordinated water molecule  $^1\text{H}_{\text{iso}}$ , which were obtained from the fitting of the NMRD profiles and DFT calculations. Finally, the analysis of the data provided information on the exchange rate of coordinated water molecules, which display mean residence times of  $\sim 7$ –17  $\mu\text{s}$  at 298 K.

Received 12th December 2022,  
Accepted 20th January 2023

DOI: 10.1039/d2qi02635j

[rsc.li/frontiers-inorganic](http://rsc.li/frontiers-inorganic)

## Introduction

Magnetic molecules are next-generation components in many different technological areas, ranging from magnetic resonance imaging (MRI)<sup>1–3</sup> to quantum information technologies.<sup>4,5</sup> All of these applications require the modulation of the spin-lattice (longitudinal) relaxation time ( $T_1^e$ ) and the phase-memory relaxation time ( $T_m^e$ ).  $T_1^e$  defines the lifetime of an excited spin state and is the upper limit of  $T_m^e$ .  $T_m^e$  is the lifetime of the electron spin superposition or coherence time, and encompasses  $T_2^e$  and all other processes that

cause electron spin dephasing. Applications in quantum information technology require designing systems where both these parameters are long, which is challenging due to the ubiquitous spin bath (nearby electronic spins or nuclear spins) that produces stochastic interactions that shorten both relaxation times.<sup>6</sup> On the other hand, contrast agents for application in MRI should be efficient at shortening the nuclear relaxation times of water proton nuclei in their vicinity.<sup>7</sup> Vanadium(IV) complexes are being actively studied as potential candidates for molecular spin qubits,<sup>8–14</sup> and have also been proposed as potential MRI contrast agents.<sup>15</sup> In the latter case, the paramagnetic V(IV) complex creates a local fluctuating magnetic field that increases the relaxation efficiency of nearby solvent protons. Vanadium(IV) has an electron spin  $S = 1/2$  and a nuclear spin  $I = 7/2$  for the stable isotope  $^{51}\text{V}$ , which presents a natural abundance of nearly 100%. Oxovanadium(IV) complexes, in particular, have longer electron spin decoherence times than many other first-row transition metal ions, a key property for applications in quantum information processing. The relaxivity induced by  $\text{VO}^{2+}$  compounds is lower than that by low molecular weight gadolinium complexes, but it

<sup>a</sup>Department of Chemistry, University of Turin, Via Giuria 9, 10125 Torino, Italy.  
E-mail: [mario.chiesa@unito.it](mailto:mario.chiesa@unito.it)

<sup>b</sup>Dipartimento di Scienze e Innovazione Tecnologica, Università del Piemonte Orientale, Viale T. Michel 11, 15121 Alessandria, Italy.  
E-mail: [mauro.botta@uniupo.it](mailto:mauro.botta@uniupo.it)

<sup>c</sup>Universidad da Coruña, Centro de Investigaciones Científicas Avanzadas (CICA) and Departamento de Química, Facultade de Ciencias, 15071 A Coruña, Galicia, Spain.  
E-mail: [carlos.platas.iglesias@udc.es](mailto:carlos.platas.iglesias@udc.es)

<sup>†</sup>Electronic supplementary information (ESI) available: Additional EPR data and geometries obtained with DFT. See DOI: <https://doi.org/10.1039/d2qi02635j>

still provides significant relaxation enhancement, particularly at low magnetic field strengths.<sup>15,16</sup> Mustafi *et al.*<sup>17</sup> reported the use of bis(acetylacetone)oxovanadium(IV) ( $[\text{VO}(\text{acac})_2]$ ) as a potential contrast agent and studied the interaction of the complex with serum albumin and performed *in vivo* experiments for imaging tumours in rats. Furthermore, vanadium(IV) complexes are used in other medical applications, such as the treatment of diabetes, anti-tumour therapy and the treatment of viral, bacterial or parasitic infections.<sup>18</sup>

The study of the NMR spectra of paramagnetic species is limited by the shortening of the nuclear transverse relaxation time ( $T_2^*$ ) caused by the presence of unpaired electrons, which may induce extensive line-broadening. If  $T_2^*$  is long enough, it is possible to observe the NMR spectra characterized by paramagnetically shifted signals. However, short  $T_2^*$  values make signals too broad to be detected. The Fast-Field-Cycling NMR (FFC-NMR) technique was designed to overcome this limitation, as it permits one to study the structural and dynamic properties of paramagnetic complexes dissolved in a solvent (usually in  $\text{H}_2\text{O}$ ), by investigating the solvent magnetic properties.<sup>19</sup> This technique is largely used for the development of new contrast agents for MRI applications.<sup>20</sup>

The effect of the paramagnetic complex on water proton relaxation is influenced by many parameters. The observed relaxation effect is the result of two main contributions: the outer-sphere contribution,<sup>21,22</sup> arising from water molecules diffusing in the proximity of the paramagnetic centre, and the inner-sphere contribution, arising from water molecules coordinated to the paramagnetic centre that get exchanged with bulk water molecules. The theoretical description of the relaxation theory is given by the Solomon–Bloembergen–Morgan equations,<sup>7</sup> and includes a rather large number of structural and dynamic parameters. Thus, it is very important to combine different techniques offering complementary information on the most important ones.<sup>23</sup>

In this paper, we report a combined EPR and  $^1\text{H}$  relaxometry study on a series of oxovanadium(IV) complexes that establishes a clear relationship between their relaxation properties and their structural and dynamic parameters (electron spin relaxation times, rotational dynamics, hydration state, water exchange rate, *etc.*). For this purpose we re-investigated the  $[\text{VO}(\text{H}_2\text{O})_5]^{2+}$  complex, which was characterized earlier using either FFC-NMR<sup>16</sup> or EPR<sup>24</sup> measurements, but not combining the two techniques. Additionally, we selected a series of complexes that contain a water molecule coordinated to the metal ion either axially ( $[\text{VO}(\text{acac})_2]$ ) or equatorially ( $[\text{VO}(\text{nta})]^-$ ,  $\text{H}_3\text{nta}$  = nitrilotriacetic acid;  $[\text{VO}(\text{ox})]^{2-}$ ,  $\text{H}_2\text{ox}$  = oxalic acid). Furthermore, we also investigated the  $[\text{VO}(\text{dtpa})]^{3-}$  complex ( $\text{H}_5\text{dtpa}$  = diethylenetriaminepentaacetic acid), which lacks any coordinated water molecule. Fig. 1 shows the models of the structures of the complexes investigated in this work obtained with DFT calculations. The analysis of the  $^1\text{H}$  nuclear magnetic relaxation dispersion (NMRD)<sup>25</sup> profiles is supported by complementary information extracted by EPR (rotational correlation times ( $\tau_{\text{R}}$ ),<sup>26</sup> longitudinal ( $T_1^*$ )<sup>27</sup> and transverse ( $T_{\text{m}}^*$ )<sup>28</sup> relaxations). Additionally, theoretical calculations based

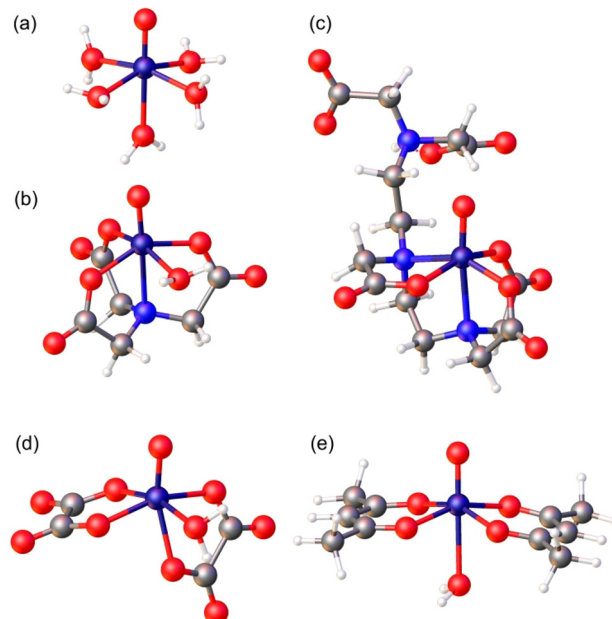


Fig. 1 Structures of the complexes investigated in this work optimized with DFT calculations (TPSSh/Def2-TZVPP): (a)  $[\text{VO}(\text{H}_2\text{O})_5]^{2+}$ , (b)  $[\text{VO}(\text{nta})(\text{H}_2\text{O})]^-$ , (c)  $[\text{VO}(\text{Hdtpa})]^{2-}$ , (d)  $[\text{VO}(\text{ox})_2(\text{H}_2\text{O})]^{2-}$ , and (e)  $[\text{VO}(\text{acac})_2(\text{H}_2\text{O})]$ .

on DFT and wave function approaches were used as an additional source of information. This integrated approach offers, for the first time, a clear description of the relaxometric behaviour of oxovanadium(IV) complexes in solution.

## Results and discussion

### Continuous wave (CW) EPR experiments

The EPR spectra of the vanadium complexes recorded in water frozen solution (77 K) show the expected eight-fold hyperfine splitting typical of  $\text{V}^{\text{IV}}$  ( ${}^5\text{V}$   $I = 7/2$ , natural abundance 99.76%).<sup>29</sup> The spectra could be simulated using the spin Hamiltonian shown in eqn (1), which considers the electronic Zeeman interaction and the hyperfine coupling of electronic and nuclear moments.

$$\mathcal{H} = \mu_{\text{B}} \hat{\mathbf{B}}^{\text{T}} \cdot \mathbf{g} \cdot \hat{\mathbf{S}} + \hat{\mathbf{S}}^{\text{T}} \cdot \mathbf{A} \cdot \hat{\mathbf{I}} \quad (1)$$

Here,  $\mathbf{g}$  is the electronic anisotropic Landé tensor and  $\mathbf{A}$  is the hyperfine coupling tensor. Computer simulation afforded the parameters reported in Table 1, while the experimental and simulated spectra are presented in Fig. 2. The  $[\text{VO}(\text{H}_2\text{O})_5]^{2+}$  complex is characterised by axially symmetric  $\mathbf{g}$ - and  $\mathbf{A}$ -tensors that match well those reported previously.<sup>24,30</sup> All other complexes show slightly rhombic tensors.

As noted previously for  $\text{VO}^{2+}$  complexes,<sup>31</sup> the values of  $g_z$  and  $A_z$  are correlated, with  $[\text{VO}(\text{H}_2\text{O})_5]^{2+}$  displaying the most negative  $A_z$  value and the lowest  $g_z$ . Detailed structural studies concluded that  $[\text{VO}(\text{acac})_2]$  is present in solution as a mixture of *cis* and *trans* isomers, with the major species in solution

**Table 1** Spin-Hamiltonian parameter of VO-complexes ( $A$ -tensor in MHz), rotational correlation times ( $\tau_R^{298}$ , ps) and activation energies for rotation ( $E_r$ , kJ mol $^{-1}$ ) obtained from CW EPR spectra simulations. The sign of the experimental hyperfine components has been taken based on the DFT results

|   |                    | $g_x$  | $g_y$  | $g_z$  | $A_x$  | $A_y$  | $A_z$ | $\tau_R^{298}$ | $E_r$          |
|---|--------------------|--------|--------|--------|--------|--------|-------|----------------|----------------|
| $[\text{VO}(\text{H}_2\text{O})_5]^{2+}$                                      | Exp.               | 1.9786 | 1.9786 | 1.9344 | -206.5 | -206.5 | -546  | $47.8 \pm 1.4$ | $14.8 \pm 0.8$ |
|   | Calc.              | 1.9830 | 1.9820 | 1.9099 | -201   | -198   | -552  |                |                |
| $[\text{VO}(\text{nta})]^-$   | Exp.               | 1.9820 | 1.9770 | 1.9375 | -203   | -187   | -527  | $35.5 \pm 1.3$ | $14.9 \pm 1.0$ |
| $[\text{VO}(\text{nta})(\text{H}_2\text{O})]^-$                               | Calc.              | 1.9805 | 1.9751 | 1.9164 | -164   | -164   | -509  |                |                |
| $[\text{VO}(\text{nta})(\text{H}_2\text{O})]^- \cdot 2\text{H}_2\text{O}$     | Calc.              | 1.9803 | 1.9761 | 1.9194 | -163   | -162   | -507  |                |                |
| $[\text{VO}(\text{dtpa})]^{3-}$   | Exp.               | 1.9822 | 1.9770 | 1.9444 | -184   | -176   | -507  | $86.0 \pm 2.2$ | $13.0 \pm 0.7$ |
| $[\text{VO}(\text{Hdtpa})]^{2-}$  | Calc.              | 1.9798 | 1.9789 | 1.9253 | -151   | -146   | -492  |                |                |
| $[\text{VO}(\text{ox})_2]^{2-}$   | Exp.               | 1.9801 | 1.9760 | 1.9392 | -192   | -181   | -520  | $38.2 \pm 0.9$ | $16.4 \pm 0.6$ |
| $[\text{VO}(\text{ox})_2(\text{H}_2\text{O})]^{2-}$                           | Calc. <sup>a</sup> | 1.9819 | 1.9777 | 1.9172 | -165   | -155   | -507  |                |                |
| $[\text{VO}(\text{ox})_2(\text{H}_2\text{O})]^{2-} \cdot 2\text{H}_2\text{O}$ | Calc. <sup>a</sup> | 1.9795 | 1.9762 | 1.9173 | -155   | -149   | -500  |                |                |
| $[\text{VO}(\text{acac})_2]$  | Exp.               | 1.9805 | 1.9735 | 1.9444 | -161   | -176   | -498  | $77.0^c$       |                |
| $[\text{VO}(\text{acac})_2(\text{H}_2\text{O})]$                              | Calc. <sup>b</sup> | 1.9855 | 1.9743 | 1.9368 | -131   | -157   | -491  |                |                |
| $[\text{VO}(\text{acac})_2(\text{H}_2\text{O})] \cdot 2\text{H}_2\text{O}$    | Calc. <sup>b</sup> | 1.9817 | 1.9758 | 1.9305 | -146   | -161   | -496  |                |                |

<sup>a</sup> Data obtained for the *cis* isomer. DLPNO-CCSD calculations afford  $A_x$ ,  $A_y$  and  $A_z$  values of -156, -148 and -509 for  $[\text{VO}(\text{ox})_2(\text{H}_2\text{O})]^{2-}$ . <sup>b</sup> Data obtained for the *trans* isomer. <sup>c</sup> Value estimated from the spectrum recorded at room temperature.

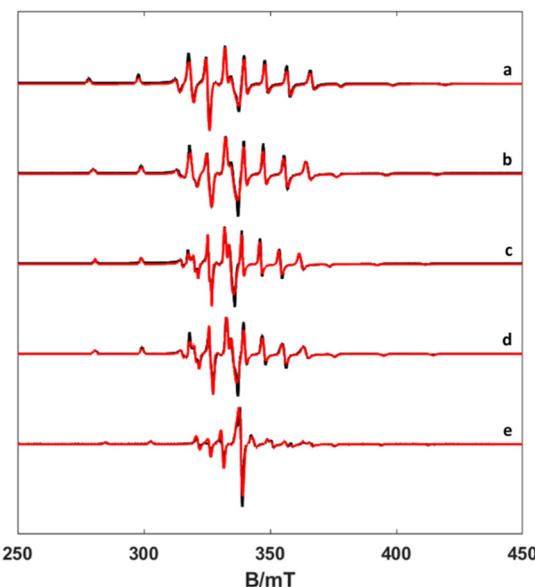


**Fig. 2** X-band CW EPR spectra of frozen solutions of complexes (a)  $[\text{VO}(\text{H}_2\text{O})_5]^{2+}$ , (b)  $[\text{VO}(\text{nta})(\text{H}_2\text{O})]^-$ , (c)  $[\text{VO}(\text{Hdtpa})]^{2-}$ , (d)  $[\text{VO}(\text{ox})_2(\text{H}_2\text{O})]^{2-}$ , and (e)  $[\text{VO}(\text{acac})_2(\text{H}_2\text{O})]$  (experimental black line, simulation red one) at 77 K, 1 mW power and 0.2 mT modulation amplitude.

being the *trans* form (~85%), which contains a water molecule coordinated in the *trans* position with respect to the oxo group.<sup>32</sup> The value of the  $^{51}\text{V}$  isotropic hyperfine coupling  $a_{\text{iso}}$  determined here for  $[\text{VO}(\text{acac})_2]$  (-278 MHz) is in excellent agreement with that reported previously for the *trans* isomer (-276 MHz), while the *cis* isomer (minor) is characterized by a larger  $a_{\text{iso}}$  value of -291 MHz.<sup>32</sup> The X-ray crystal structures of the  $[\text{VO}(\text{ox})_2]^{2-}$  and  $[\text{VO}(\text{nta})]^-$  complexes show that a water molecule is coordinated to the metal ion in the *cis* position with respect to the oxo group.<sup>33-35</sup> The X-ray structure of the  $[\text{VO}(\text{H}_3\text{DTPA})]$  complex evidences coordination of the ligand through two amine N atoms and three oxygen atoms of carbox-

ylate groups, and thus this complex lacks any coordinated water molecule.<sup>36</sup>

### Variable temperature EPR experiments

EPR spectra were recorded in aqueous solutions in the temperature range 294–353 K. Under these circumstances, the anisotropic  $g$ - and  $A$ -tensors are averaged out depending on the rate of motion of the complex, which in turn depends on the temperature. The result is an 8-line spectrum centred at the average  $g$  factor and line separation reflecting the  $^{51}\text{V}$  isotropic hyperfine component  $a_{\text{iso}}$ . Inspection of Fig. 3 shows a clear  $m_l$  linewidth dependency, which is directly correlated with the rotational correlation time ( $\tau_R$ ). Using the rigid limit spin-Hamiltonian parameters reported in Table 1,  $\tau_R$  was determined through the

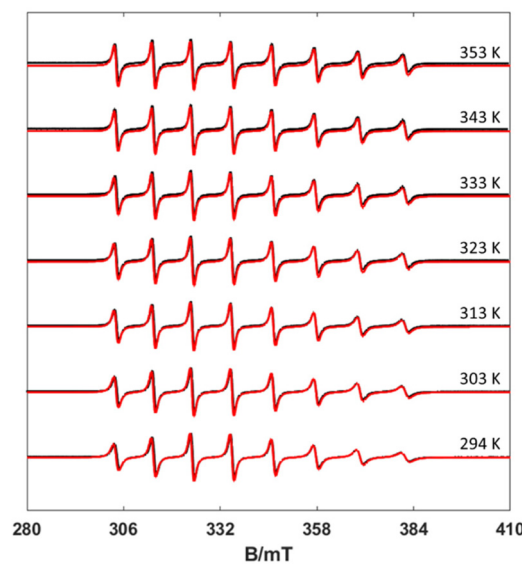


**Fig. 3** Experimental (black) and simulated (red) X-band CW EPR spectra of the  $[\text{VO}(\text{nta})]^-$  complex recorded at different temperatures (10 mW power and 0.5 mT modulation amplitude).

simulation of the spectra using the Easyspin<sup>26</sup> routine *garlic* (Fig. 3, see also Fig. S1–S3, ESI†). In this way, the spectra are simulated leaving  $\tau_R$  as a unique free parameter.

The  $\tau_R$  values measured at different temperatures are summarized in Table S1 (ESI).† The values of  $\tau_R$  decrease upon increasing the temperature, as would be expected, following a simple exponential dependence according to the below equation (Fig. S4 and S5, ESI†):

$$\tau_R = \tau_R^{298} \exp \left\{ \frac{E_R}{R} \left( \frac{1}{T} - \frac{1}{298.15} \right) \right\}. \quad (2)$$

In eqn (2),  $\tau_R^{298}$  is the rotational correlation time at 298.15 K and  $E_R$  represents the corresponding activation energy for rotation. The longest  $\tau_R^{298}$  value was determined for the complex with H<sub>5</sub>dtpa, as expected according to its molecular weight. The  $\tau_R^{298}$  value determined for this complex is slightly lower than that determined by Chen using EPR measurements (~105 ps).<sup>15</sup> The [VO(ox)<sub>2</sub>]<sup>2-</sup> and [VO(nta)]<sup>-</sup> complexes present comparable molecular weights and very similar rotational correlation times. However, the [VO(acac)<sub>2</sub>] complex displays a longer  $\tau_R^{298}$  value than the latter two, in spite of their similar molecular weight. The [VO(H<sub>2</sub>O)<sub>5</sub>]<sup>2+</sup> complex presents a  $\tau_R^{298}$  value somewhat longer than those of [VO(ox)<sub>2</sub>]<sup>2-</sup> and [VO(nta)]<sup>-</sup>, which can be attributed to the formation of a well-defined second-sphere hydrogen-bonding network. The activation energies for rotation (~15 kJ mol<sup>-1</sup>) are similar to those obtained from relaxometric data for the aqua-complexes of Gd (III),<sup>37</sup> Mn(II)<sup>38</sup> and Fe(III)<sup>39</sup> complexes.

### Electron spin dynamics: $T_1^e$ and $T_m^e$ measurements

To investigate the temperature dependence of the electronic relaxation times of the VO<sup>2+</sup> complexes, Q-band ESE spectra were recorded using a standard Hahn echo sequence. Representative spectra recorded at 10 K are shown in Fig. 4,

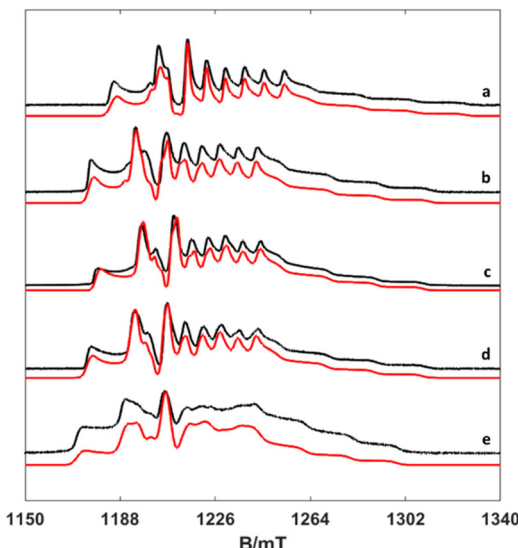


Fig. 4 Experimental (black) and simulated (red) Q-band ESE spectra (a) [VO(H<sub>2</sub>O)<sub>5</sub>]<sup>2+</sup>, (b) [VO(nta)(H<sub>2</sub>O)]<sup>-</sup>, (c) [VO(Hdtpa)]<sup>2-</sup>, (d) [VO(ox)<sub>2</sub>(H<sub>2</sub>O)]<sup>2-</sup>, and (e) [VO(acac)<sub>2</sub>(H<sub>2</sub>O)].

along with the corresponding computer simulations. The spin Hamiltonian parameters obtained from the analysis of the CW-X-band EPR spectra provide a good simulation of the Q-band ESE spectra, adding confidence on the values reported in Table 1. The electron spin relaxation times were measured at a fixed magnetic field, corresponding to the maximum echo intensity. To investigate the spin relaxation times in detail and to quantify the electronic phase memory time and the spin-lattice relaxation time in frozen solutions as a function of temperature, echo decay and inversion recovery experiments were performed in the temperature range 20–200 K. The corresponding values are shown in Fig. 5. For [VO(acac)<sub>2</sub>] the echo relaxation is too fast to allow accurate measurements above 120 K. The  $T_1^e$  values were obtained using inversion-recovery experiments and by subsequent fitting of the signal intensity ( $I$ ) to a bi-exponential equation:

$$I = I_0 + k_m \exp \left[ -\left( \frac{t}{T_1^e} \right) \right] + k_n \exp \left[ -\left( \frac{t}{T_1^e} \right) \right]. \quad (3)$$

The values of the pre-exponential factors  $k_m$  and  $k_n$  indicate that the long  $T_1^e$  component dominates the inversion-recovery traces (Table S2, ESI†). The  $T_1^e$  values decrease steadily on increasing the temperature, with  $T_1^e$  being in the range ~40–2100  $\mu$ s at 20 K and decreasing to ca. 6–15  $\mu$ s at 80 K. The plots of  $\log T_1^e$  versus  $\log T$  are linear, which indicates that relaxation is dominated by the Raman mechanism according to eqn (4), where  $b$  and  $n$  are the Raman coefficient and Raman exponent, respectively. Thus, direct relaxation appears to be negligible in the temperature range explored here.

$$\frac{1}{T_1^e} = bT^n \quad (4)$$

The fit of the data (Table 2) afforded similar  $n$  values of 3.0–3.3 for [VO(H<sub>2</sub>O)<sub>5</sub>]<sup>2+</sup>, [VO(ox)<sub>2</sub>]<sup>2-</sup> and [VO(DTPA)]<sup>3-</sup>, as can be anticipated by the similar slopes of the plots shown in Fig. 5. These  $n$  values are close to those determined for different oxovanadium(IV) complexes using magnetic suscepti-

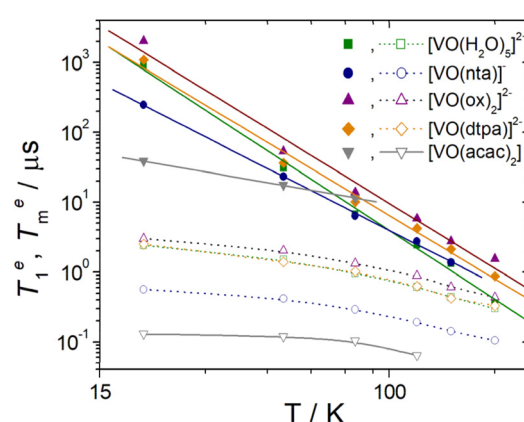


Fig. 5 Temperature dependence of  $T_1^e$  (filled symbols) and  $T_m^e$  (hollow symbols) for the oxovanadium(IV) complexes studied in this work. The solid lines correspond to the fits of the data to a Raman type of relaxation (see the text). Dotted lines are a guide to the eye.



**Table 2** Results of the fits of  $T_1^e$  data according to eqn (4)<sup>a</sup>

|  | $b/\mu\text{s}^{-1} \text{K}^{-n}$ | $n$     |
|--|------------------------------------|---------|
| $[\text{VO}(\text{H}_2\text{O})_5]^{2+}$ | $6.8(5) \times 10^{-8}$            | 3.3(1)  |
| $[\text{VO}(\text{nta})]^-$              | $1.95(8) \times 10^{-6}$           | 2.57(5) |
| $[\text{VO}(\text{dtpa})]^{3-}$          | $6.8(6) \times 10^{-8}$            | 3.1(2)  |
| $[\text{VO}(\text{ox})_2]^{2-}$          | $1.4(2) \times 10^{-7}$            | 3.0(1)  |
| $[\text{VO}(\text{acac})_2]$             | $1.86(4) \times 10^{-3}$           | 0.88(2) |

<sup>a</sup> Data obtained from frozen aqueous solutions (complex concentration  $\sim 3 \text{ mM}$ ).

bility and EPR measurements.<sup>9,10,40,41</sup> The  $[\text{VO}(\text{nta})]^-$  complex is characterised by a slightly lower  $n$  value, while  $[\text{VO}(\text{acac})_2]$  displays a very low  $n$  value of 0.88. As a result,  $T_1^e$  decreases much smoothly with temperature for  $[\text{VO}(\text{acac})_2]$  compared to all other complexes studied here. As a result,  $[\text{VO}(\text{acac})_2]$  shows the shortest  $T_1^e$  value (38.7  $\mu\text{s}$ ) among the five complexes at 20 K, but all five complexes show similar  $T_1^e$  values at 80 K (6–14  $\mu\text{s}$ ). The different temperature dependence of  $T_1^e$  observed for  $[\text{VO}(\text{acac})_2]$  is likely related to its *trans* coordination geometry, where the donor atoms of the acac ligands occupy equatorial positions.

For  $T_m^e$  measurements the decay traces were fitted using the stretched-exponential expression:

$$I = I_0 + k_m \exp\left(-\frac{2\tau_p}{T_m^e}\right)^{\beta_m} \quad (5)$$

Here,  $I$  is the echo intensity,  $2\tau_p$  is the time delay between the initial and echo detection pulses, and  $\beta_m$  is the stretch factor. The values of  $T_m^e$  decrease smoothly with temperature for all complexes, with  $[\text{VO}(\text{H}_2\text{O})_5]^{2+}$ ,  $[\text{VO}(\text{ox})_2]^{2-}$  and  $[\text{VO}(\text{dtpa})]^{3-}$  being characterized by similar and relatively long values. The  $[\text{VO}(\text{acac})_2]$  complex is characterized by the shortest values of  $T_m^e$ , with  $[\text{VO}(\text{nta})]^-$  showing an intermediate behaviour. Thus, the trend in  $T_m^e$  values resembles that observed for  $T_1^e$  at a low temperature (20 K).

### <sup>1</sup>H nuclear relaxation dispersion (NMRD) profiles

The NMRD profiles of the oxovanadium(IV) complexes were measured at various temperatures (283, 298 and 310 K) from 0.01 to 120 MHz (expressed as a function of <sup>1</sup>H Larmor frequency). For each NMRD profile, 25 relaxation times were measured, in order to have a good definition of the curves (Fig. 6).

The NMRD profiles obtained for the  $[\text{VO}(\text{H}_2\text{O})_5]^{2+}$  complex present a similar shape to that reported by Bertini *et al.*<sup>16</sup> Relaxivity ( $r_1$ ) is nearly constant at low fields in the range from 0.01 to 0.1–0.2 MHz. A dispersion in which  $r_1$  decreases is observed above  $\sim 0.2$  MHz until 20 MHz, followed by a region with constant  $r_1$  at frequencies above 20 MHz. The NMRD profiles recorded for the  $[\text{VO}(\text{acac})_2]$  and  $[\text{VO}(\text{ox})_2]^{2-}$  complexes show similar shapes. The shape of the NMRD profile is however different for the  $[\text{VO}(\text{nta})]^-$  complex, which shows a broad region of constant relaxivity below 2 MHz and a dispersion in the 2–30 MHz region. This shape is characteristic of

complexes where the inner-sphere contribution to relaxivity is dominated by the dipolar mechanism, such as  $\text{Gd}^{3+}$  and most  $\text{Mn}^{2+}$  complexes.<sup>20</sup> The relaxivity increase observed below  $\sim 1$  MHz denotes the presence of a significant scalar contribution, as observed for  $[\text{Mn}(\text{H}_2\text{O})_6]^{2+}$  and a few other  $\text{Mn}^{2+}$  complexes.<sup>38,42,43</sup>

The scalar contribution that dominates  $r_1$  at low fields depends on the isotropic (Fermi contact) proton hyperfine coupling constant  $^H\alpha_{\text{iso}}$  and the correlation time  $1/\tau_{\text{si}}$ , which is the sum of the water exchange rate constant ( $k_{\text{ex}} = 1/\tau_{\text{M}}$ ) and the electronic longitudinal ( $1/T_1^e$ ) or transverse ( $1/T_2^e$ ) relaxation rates. The electronic relaxation times are generally nearly invariant in the temperature range used for NMRD measurements. The increase of relaxivity at low frequencies observed for  $[\text{VO}(\text{H}_2\text{O})_5]^{2+}$  and  $[\text{VO}(\text{ox})_2]^{2-}$  as a function of temperature indicates that  $r_1$  is limited by a slow water exchange rate, as  $\tau_{\text{M}}$  is longer than  $T_1$  for the coordinated water molecule. Increasing temperature decreases  $\tau_{\text{M}}$  for the proton nuclei of the coordinated water, and thus  $r_1$  increases.

At high frequencies, the inner-sphere contribution to  $r_1$  is provided by the dipolar mechanism, for which the relevant correlation time involves  $\tau_{\text{M}}$ ,  $T_i^e$  ( $T_1^e$ ,  $T_2^e$ ) and  $\tau_{\text{R}}$ . The shortest among these three correlation times is  $\tau_{\text{R}}$ , which is in the ps time scale, while  $\tau_{\text{M}}$  and  $T_i^e$  appear to be in the  $\mu\text{s}$  and  $\text{ns}$  time scales, respectively. Thus, the fast rotation of the complex in solution limits  $r_1$  at high fields, and therefore the trend with temperature is reversed, as  $\tau_{\text{R}}$  becomes shorter with increasing temperature.

The  $[\text{VO}(\text{nta})]^-$  complex presents higher  $r_1$  values than the complex with H<sub>5</sub>DTPA over the whole range of proton Larmor frequencies. This suggests that the  $[\text{VO}(\text{nta})]^-$  complex contains a coordinated water molecule, as observed in the solid state.<sup>35</sup> The complex with H<sub>5</sub>DTPA likely lacks any coordinated water molecule, with the observed relaxivity being a consequence of the outer-sphere mechanism. The decrease in relaxivity with temperature is therefore likely related to a faster diffusion.

### Theoretical calculations

DFT calculations were carried out to gain insight into the structures of the complexes in solution and their correlation with EPR parameters. The geometries of the complexes were optimized at the TPSSh/Def2-TZVPP level incorporating bulk solvent effects with a polarized continuum model (see Computational details below). The optimized molecular geometries are presented in Fig. 1, while relevant structural features are provided in Table 3 (see also Tables S4–S11, ESI†).

The  $[\text{VO}(\text{H}_2\text{O})_5]^{2+}$  system is characterized by short V–O<sub>cis</sub> distances and a long V–O<sub>trans</sub> distance associated with the *trans* influence of the V=O bond. The calculated distances are in excellent agreement with the experimental values obtained with X-ray diffraction measurements.<sup>44–46</sup> The calculated V=O distance (1.565 Å) is also in nice agreement with the X-ray data (1.57–1.58 Å). DFT calculations were also performed in the  $[\text{VO}(\text{oxa})_2(\text{H}_2\text{O})]^{2-}$  system, for which X-ray structures were reported with the coordinated water molecule at both *cis*<sup>33,47</sup>



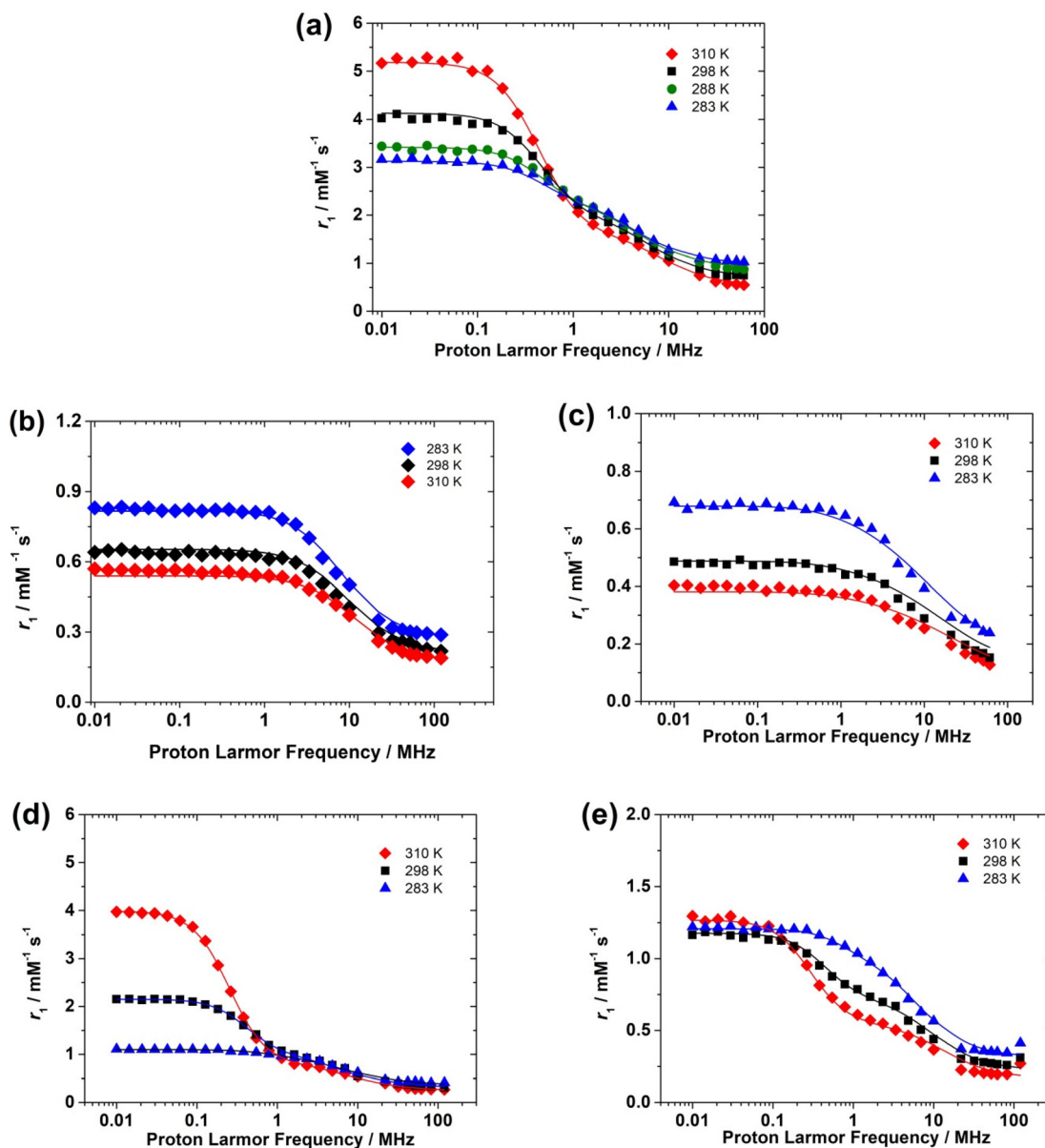


**Fig. 6**  $^1\text{H}$  Nuclear Magnetic Relaxation Dispersion (NMRD) profiles recorded at different temperatures for (a)  $[\text{VO}(\text{H}_2\text{O})_5]^{2+}$  ( $\text{pH} = 0.7$ ), (b)  $[\text{VO}(\text{nta})]^-$  ( $\text{pH} = 5.5$ ), (c)  $[\text{VO}(\text{Hdtpa})]^{2-}$  ( $\text{pH} = 7.0$ ), (d)  $[\text{VO}(\text{oxa})_2]^{2-}$  ( $\text{pH} = 5.5$ ) and (e)  $[\text{VO}(\text{acac})_2]$  ( $\text{pH} = 5.6$ ). The solid lines correspond to the fits of the data as explained in the text.

and *trans*<sup>48</sup> positions with respect to the  $\text{V}=\text{O}$  bond. The calculations on the *trans* isomer systematically led to square pyramidal optimized geometries, even upon the inclusion of two explicit second-sphere water molecules. The  $^1\text{H}$  NMRD data clearly show the presence of a water molecule coordinated to the  $\text{VO}^{2+}$  cation, and thus subsequent calculations were performed on the *cis* isomer (Table 3). The DFT calculations provide a  $\text{V}-\text{O}_{\text{water}}$  distance that is considerably longer than that observed in the solid state. The inclusion of two explicit second-sphere water molecules shortens the  $\text{V}-\text{O}_{\text{water}}$  distance by  $\sim 0.04$  Å, but the calculated value remains 0.11 Å longer than the X ray value.

Calculations performed in the  $[\text{VO}(\text{nta})(\text{H}_2\text{O})]^-$  system provide a minimum energy conformation with the coordinated water molecule in the *cis* position and the N atom of nitrilotriacetate occupying the *trans* position, which leads to a long  $\text{V}-\text{N}$  distance (2.372 Å) associated with the *trans* influence of the  $\text{V}=\text{O}$  bond. This is in good agreement with the X-ray structures reported in the literature.<sup>34,35</sup> Again, the inclusion of explicit second-sphere water molecules causes a shortening of the  $\text{V}-\text{O}_{\text{water}}$  distance, as observed previously for  $\text{Mn}(\text{II})$  and  $\text{Gd}(\text{III})$  complexes.<sup>51,52</sup>

DFT calculations yield two minimum energy geometries for the  $[\text{VO}(\text{acac})(\text{H}_2\text{O})]$  system characterized by *cis* and *trans*



**Table 3** Distances (Å) and  $^1\text{H}$  hyperfine coupling constants  $^{\text{H}}\text{a}_{\text{iso}}$  (MHz) of coordinated water molecules obtained with DFT calculations at the TPSSh/Def2-TZVPP level and values reported in the literature

|   |                   | V=O    | V-O         | V-O <sub>H<sub>2</sub>O</sub>                | V-N         | V...H <sub>H<sub>2</sub>O</sub>        | $^{\text{H}}\text{a}_{\text{iso}}$        | Ref.      |
|---|-------------------|--------|-------------|--|-------------|--|---|-----------|
| [VO(H <sub>2</sub> O) <sub>5</sub> ] <sup>2+</sup>  | DFT               | 1.565  |             | 2.052–2.056; <sup>c</sup> 2.212 <sup>d</sup> |             | 2.671 <sup>c</sup> /2.888 <sup>d</sup> | 0.73–7.86 <sup>c</sup> /0.09 <sup>d</sup> |           |
|   | Exp.              | 1.569  |             | 2.023–2.030; <sup>c</sup> 2.183 <sup>d</sup> |             |  | –0.39–8.67 <sup>c</sup>                   | 46 and 49 |
|   |                   | 1.577  |             | 2.026–2.027; <sup>c</sup> 2.175 <sup>d</sup> |             |  | –0.04; 0.01 <sup>d</sup>                  | 44        |
| [VO(nta)(H <sub>2</sub> O)] <sup>–</sup><br>[VO(nta)(H <sub>2</sub> O)] <sup>–</sup> ·2H <sub>2</sub> O                             | DFT               | 1.606  | 1.974–1.979 | 2.128  | 2.372       | 2.682                                  | 3.89                                      |           |
|   | DFT               | 1.605  | 1.988–1.999 | 2.085  | 2.368       | 2.587                                  | 4.90                                      |           |
|   | Exp.              | 1.596  | 1.997–2.022 | 2.005  | 2.322       |  |   | 35        |
| [VO(Hdtpa)] <sup>2–</sup>   | DFT               | 1.6112 | 1.987–1.994 | —  | 2.209/2.356 | —                                      | —   |           |
|   | Exp.              | 1.603  | 1.981–2.032 |  | 2.179/2.304 |  |   | 36        |
| [VO(ox) <sub>2</sub> (H <sub>2</sub> O)] <sup>2–</sup><br>[VO(ox) <sub>2</sub> (H <sub>2</sub> O)] <sup>2–</sup> ·2H <sub>2</sub> O | DFT <sup>a</sup>  | 1.613  | 1.973–2.151 | 2.186  |             | 2.667                                  | 4.30; 1.34                                |           |
|   | DFT <sup>a</sup>  | 1.629  | 1.974–2.130 | 2.141  |             | 2.732                                  | 1.6; 1.72                                 |           |
|   | Exp. <sup>a</sup> | 1.594  | 2.006–2.184 | 2.033  |             |  |   | 33        |
| [VO(acac) <sub>2</sub> (H <sub>2</sub> O)]<br>[VO(acac) <sub>2</sub> (H <sub>2</sub> O)]·2H <sub>2</sub> O                          | DFT <sup>b</sup>  | 1.597  | 1.991–1.999 | 2.479  | —           | 2.950                                  | 0.04                                      |           |
|   | DFT <sup>b</sup>  | 1.598  | 1.991–2.026 | 2.336  | —           | 2.868                                  | 0.07                                      |           |
|   | Exp. <sup>b</sup> | 1.599  | 1.982–1.998 | 2.196  | —           |  |   | 50        |

<sup>a</sup> Data obtained for the *cis* isomer. <sup>b</sup> Data obtained for the *trans* isomer. <sup>c</sup> Data for equatorial water molecules. The range of experimental hyperfine couplings refers to the four inequivalent equatorial water protons obtained by DFT (this work) or determined in the ENDOR single crystal study of ref. 49. <sup>d</sup> Data for axial water molecules. The two protons of the axial water molecule are not magnetically equivalent.

coordination of the water molecule. The relative Gibbs free energies calculated with DFT favour the *trans* isomer by 4.1 kcal mol<sup>–1</sup>. The relative energy is reversed and reduced to 0.3 kcal mol<sup>–1</sup> upon inclusion of two second-sphere water molecules, and thus both forms likely have a significant population in solution. This is in line with EPR measurements, which evidenced the presence of the *cis* and *trans* isomers in solution.<sup>32,53</sup> As expected, the *trans* isomer displays a long V–O<sub>water</sub> distance of 2.48 Å. This distance was found to be up to ~0.27 Å shorter in the solid state.<sup>50</sup> Inclusion of explicit second-sphere water molecules brings this distance closer to the experimental value (Table 2). The overestimation of the V–O<sub>water</sub> distance by DFT is likely related to a rather flat potential energy surface associated with the weak interaction, which arises from the strong *trans* influence of the V=O bond.

An X-ray structure was reported for the [VO(H<sub>3</sub>DTPA)] complex, in which two acetate groups and one of the amine N atoms are protonated.<sup>36</sup> However, the first protonation constant of the [VO(DTPA)]<sup>3–</sup> complex was reported to be  $\log K = 7.0$ , and thus the main species in solution at the pH used for <sup>1</sup>H NMRD measurements corresponds to the mono-protonated form of the complex.<sup>54</sup> Thus, DFT calculations were performed in the [VO(HDTPA)]<sup>2–</sup> system. The calculated structure resembles the crystal structure of the [VO(H<sub>3</sub>DTPA)] complex.

The EPR measurements described above evidenced significant variations of the <sup>51</sup>V hyperfine coupling constants for the complexes investigated in this work (Table 1). The values of  $A_x$ ,  $A_y$  and  $A_z$  were estimated with DFT calculations using the TPSS0 functional<sup>55</sup> (25% HF exchange), a variant of the TPSSh functional<sup>56</sup> (10% exchange) with increased HF exchange. The TPSS0 functional was found to perform well in the prediction of  $A$ -tensors of V(IV) complexes.<sup>57</sup> The results obtained at the TPSS0/Def2-QZVPP level (Table 1) show that DFT predicts the

experimental hyperfine coupling constants with a rather good accuracy. Test calculations performed with the coupled cluster theory, using the recently described domain based local pair natural orbital method (DLPNO-CCSD), afforded  $A_x$ ,  $A_y$  and  $A_z$  values for [VO(ox)<sub>2</sub>(H<sub>2</sub>O)]<sup>2–</sup>, in excellent agreement with both the experiment and DFT (Table 1). The DLPNO-CCSD method was found to provide very accurate spin densities for both organic radicals<sup>58</sup> and transition metal complexes.<sup>59</sup> Furthermore, our DFT calculations reported here for [VO(H<sub>2</sub>O)<sub>5</sub>]<sup>2+</sup> and [VO(acac)(H<sub>2</sub>O)] afford very similar results to those reported recently using DLPNO-CCSD calculations.<sup>59</sup>

The [VO(H<sub>2</sub>O)<sub>5</sub>]<sup>2+</sup> system is characterized by more negative  $A_x$ ,  $A_y$  and  $A_z$  values. Furthermore, the calculated absolute  $A_z$  values follow the trend [VO(H<sub>2</sub>O)<sub>5</sub>]<sup>2+</sup> > [VO(nta)(H<sub>2</sub>O)]<sup>–</sup> > [VO(ox)<sub>2</sub>(H<sub>2</sub>O)]<sup>2–</sup> > [VO(Hdtpa)]<sup>2–</sup> > [VO(acac)(H<sub>2</sub>O)], in agreement with the experimental trend. The inclusion of explicit second-sphere water molecules has a minor impact on the  $A$ -tensor values. Thus, it is possible to conclude that DFT describes rather accurately the spin density distributions in these complexes.

In contrast to  $A$ -tensors,<sup>60</sup> the prediction of  $g$ -tensors of transition metal complexes with DFT is particularly challenging, with the results depending dramatically on the functional used and the amount of HF exchange.<sup>61,62</sup> Good agreement between the experimental  $g$ -tensor values and those obtained with DFT was observed for some V(IV) complexes.<sup>63,64</sup> For the complexes studied here, test calculations performed with different functionals showed that the prediction of  $g$ -tensors with DFT is particularly problematic. Thus, we turned our attention to calculations based on the complete active space self-consistent field (CASSCF) method [CAS(5,1)], with a dynamic correlation being introduced with the N-Electron Valence State Perturbation Theory (NEVPT2). The



*g*-tensors calculated at the CASSCF/NEVPT2 level present  $g_x$  and  $g_y$  values close to the experimental data. The calculated  $g_z$  values are somewhat lower than the experimental ones, but follow rather well the experimental trend. Indeed, [VO(acac)(H<sub>2</sub>O)] and [VO(Hdtpa)]<sup>2-</sup> display the highest  $g_z$  values among the five complexes, and then decrease following the order [VO(nta)(H<sub>2</sub>O)]<sup>-</sup> > [VO(ox)<sub>2</sub>(H<sub>2</sub>O)]<sup>2-</sup> > [VO(H<sub>2</sub>O)<sub>5</sub>]<sup>2+</sup>. As observed for the *A*-tensors, the incorporation of explicit second-sphere water molecules has a minor impact on the calculated values. Overall, the theoretical calculations presented here capture the main features observed for EPR parameters, which indicates that the molecular geometries describe reasonably well the structures of this family of complexes in solution.

### Fitting of the <sup>1</sup>H NMRD profiles

The analysis of the NMRD profiles was initiated by attempting to fit the data recorded for the [VO(HDTPA)]<sup>2-</sup> complex, as for this system  $r_1$  is expected to be the result of the outer-sphere contribution only. A previous relaxometric study presented fitting of the data using unrealistically low distances of the closest approach of outer-sphere water molecules ( $a_{V-H} \sim 2.0 \text{ \AA}$ ).<sup>15</sup> This prompted the authors of ref. 15 to introduce a second-sphere contribution to obtain more reasonable fitting parameters. We attempted to fit the data using the diffusion translational model proposed by Freed,<sup>21</sup> employing a distance of the closest approach of 2.45 Å. This distance corresponds to the average V...H distance observed in the DFT structure of [VO(ox)<sub>2</sub>(H<sub>2</sub>O)]<sup>2-</sup>·2H<sub>2</sub>O, in which a non-coordinated water molecule is involved in hydrogen bonding interaction with the V=O group. A reasonably good fit was obtained using  $a_{V-H} = 2.45 \text{ \AA}$  (Fig. 6c), affording values of the relative diffusion coefficient  $D_{V-H}^{298}$  and its activation energy  $E_D$  very similar to those obtained for other small paramagnetic complexes (Table 4).<sup>37,65,66</sup> Furthermore, the values obtained from the fits are close to those reported for the self-diffusion of water in water ( $D^{298} = 23.0 \text{ m}^2 \text{ s}^{-1}$  and  $E_D = 17.6 \text{ kJ mol}^{-1}$ ).<sup>67</sup> The fast diffusion of the small water molecule is expected to dominate the relative diffusion coefficient  $D_{V-H}^{298}$ , and thus these results provide confidence in the analysis. The  $a_{V-H}$  value of 2.45 Å

was subsequently used to fit the NMRD data of [VO(ox)<sub>2</sub>(H<sub>2</sub>O)]<sup>2-</sup> and [VO(H<sub>2</sub>O)<sub>5</sub>]<sup>2+</sup>, while for the [VO(nta)(H<sub>2</sub>O)]<sup>-</sup> and [VO(acac)(H<sub>2</sub>O)] complexes we had to use a somewhat longer value (2.7 Å) to obtain satisfactory fits. This may be related to the lower net electrical charges of the latter two complexes compared to the former. The  $a_{V-H}$  value assumed for [VO(nta)(H<sub>2</sub>O)]<sup>-</sup> and [VO(acac)(H<sub>2</sub>O)] is close to the distance between the H atom of a methanol molecule involved in hydrogen bonding with the oxo group in [VO(acac)(H<sub>2</sub>O)] (2.79 Å).<sup>68</sup> The values of  $D_{V-H}^{298}$  and  $E_D$  obtained for the [VO(HDTPA)]<sup>2-</sup> complex were subsequently fixed for the analysis of all other complexes investigated here.

We next analysed the data obtained for the [VO(nta)(H<sub>2</sub>O)]<sup>-</sup> complex, which lacks dispersion at a low field indicative of a scalar relaxation mechanism. Here the relaxivity in the high-field region is limited by  $\tau_R$ , and thus we were unable to fit the data using both  $\tau_R$  and  $k_{ex} = 1/\tau_M$  as the fitting parameters. Therefore, we fixed the values of  $\tau_R^{298}$  and the activation parameter  $E_r$  to the values obtained with EPR measurements (see above). This allowed us to obtain an estimate of  $\tau_M$ , although with a relatively large statistical error ( $14.5 \pm 3.4 \mu\text{s}$ ). The NMRD profiles of [VO(H<sub>2</sub>O)<sub>5</sub>]<sup>2+</sup>, [VO(ox)<sub>2</sub>(H<sub>2</sub>O)]<sup>2-</sup> and [VO(acac)(H<sub>2</sub>O)] could be satisfactorily fitted considering both dipolar and scalar contributions to inner-sphere relaxivity. The number of coordinated water molecules  $q$  was fixed to 4 in the case of [VO(H<sub>2</sub>O)<sub>5</sub>]<sup>2+</sup>, since the axial water molecule is very labile, with a mean residence time estimated to be  $\sim 1 \text{ ns}$ .<sup>69</sup> Thus, the axial water molecule is not expected to contribute significantly to the observed relaxivity. Finally, the distances involving the paramagnetic ion and the proton nuclei of inner-sphere water molecules were estimated from DFT calculations and fixed during the fitting procedures.

### Spin density distributions

The electron spin density at a certain nucleus N,  $\rho_N^{\alpha-\beta}$  is directly measured by the isotropic hyperfine structure constant,  $a_{iso} = \frac{2\mu_0}{3} g_e \mu_B g_n \mu_N / \rho_N^{\alpha-\beta}$  where  $\mu_0$  is the vacuum permeability,  $g_e$  is the electron *g*-factor,  $\mu_B$  is the Bohr's magneton,

**Table 4** Parameters obtained from the simultaneous analysis of <sup>1</sup>H NMRD data

|   | [VO(H <sub>2</sub> O) <sub>5</sub> ] <sup>2+</sup> | [VO(dtpa)] <sup>3-</sup> | [VO(ox) <sub>2</sub> ] <sup>2-</sup> | [VO(nta)] <sup>-</sup> | [VO(acac)] <sub>2</sub> |
|---|--|--------------------------|--------------------------------------|------------------------|-------------------------|
| $\tau_m^{298}/\mu\text{s}$                          | $16.7 \pm 0.8$                                     | —                        | $16.7 \pm 0.2$                       | $14.5 \pm 3.4$         | $6.3 \pm 0.8$           |
| $\Delta H^*/\text{kJ mol}^{-1}$                     | $19.3 \pm 1.1$                                     | —                        | $72.6 \pm 1.1$                       | $13.2 \pm 5.0$         | $8.1 \pm 4.0$           |
| $\tau_R^{298}/\text{ps}$                            | $46.1 \pm 1.0$                                     | —                        | $52.4 \pm 1.1$                       | $35.5^c$               | $30.9 \pm 2.3$          |
| $E_r/\text{kJ mol}^{-1}$                            | $25.0 \pm 1.2$                                     | —                        | $22.3 \pm 1.7$                       | $14.9^c$               | $26.4 \pm 2.7$          |
| $T_1^{298}/\text{ns}$                               | $1.08 \pm 0.11$                                    | $0.88 \pm 0.06$          | $0.88 \pm 0.03$                      | $0.31 \pm 0.08$        | $0.62 \pm 0.05$         |
| $E_s/\text{kJ mol}^{-1}$                            | $1.0^a$  | $1.0^a$                  | $22.3 \pm 2.0$                       | $12.0 \pm 5.0$         | $27.9 \pm 7.6$          |
| $D_{V-H}^{298}/10^{-10} \text{ m}^2 \text{ s}^{-1}$ | $20.2^a$   | $20.2 \pm 0.1$           | $20.2^a$                             | $20.2^a$               | $20.2^a$                |
| $E_D/\text{kJ mol}^{-1}$                            | $17.0^a$   | $17.0 \pm 1.3$           | $17.0^a$                             | $17.0^a$               | $17.0^a$                |
| ${}^H a_{iso}/\text{MHz}$                           | $3.77 \pm 0.3$                                     | —                        | $3.66 \pm 0.03$                      | —                      | $1.75 \pm 0.25$         |
| $r_{V-H}/\text{\AA}$                                | $2.671^b$  | —                        | $2.667^b$                            | $2.682^b$              | $2.678^b$               |
| $a_{V-H}/\text{\AA}$                                | $2.45^a$   | $2.45^a$                 | $2.45^a$                             | $2.70^a$               | $2.70^a$                |
| $q$   | 4  | 0                        | 1                                    | 1                      | 1                       |

<sup>a</sup> Parameters fixed during the fitting procedure. <sup>b</sup> Parameters fixed to the estimates obtained with DFT. <sup>c</sup> Values fixed to those obtained with EPR measurements.



$g_n$  is the nuclear *g* factor and  $\mu_N$  is the nuclear magneton. The spin density at the proton,  ${}^1\text{H}_{\text{iso}}$ , is one of the key parameters affecting relaxivity. It is directly measured using advanced EPR techniques, such as ENDOR (electron nuclear double resonance) and ESEEM (electron spin-echo envelope modulation), and can be estimated through the fitting of the NMRD data (Table 4). Moreover, the use of computational methods can greatly enhance their interpretation. For  $[\text{VO}(\text{H}_2\text{O})_5]^{2+}$  single crystals, ENDOR data are available, reporting small  ${}^1\text{H}_{\text{iso}}$  values of 0.01 and  $-0.04$  MHz for axially coordinated water and larger values in the range from  $-0.39$  to  $8.67$  MHz for equatorially coordinated water molecules. These data, corroborated by DFT calculations,<sup>31</sup> show that the isotropic hyperfine coupling constants of the water molecule protons are very sensitive not only to the  $\text{V}-\text{O}_{\text{H}_2\text{O}}$  distance but also crucially depend on the orientation of the molecule, with respect to the vanadyl bond. The  ${}^1\text{H}_{\text{iso}}$  values obtained in this work for the equatorial water molecules  $[\text{VO}(\text{H}_2\text{O})_5]^{2+}$  fall within the range  $0.73$ – $7.86$  MHz (Table 3), in nice agreement with the experiment. The  ${}^1\text{H}_{\text{iso}}$  value for  $[\text{VO}(\text{H}_2\text{O})_5]^{2+}$  estimated from the fitting of the NMRD data (Table 4) is of the order of  $3.7$  MHz and reflects an averaged value over different water orientations.

The average value obtained for equatorial water molecules with DFT ( ${}^1\text{H}_{\text{iso}} = 4.0$  MHz) is in excellent agreement with the result obtained with NMRD. Similar values ( ${}^1\text{H}_{\text{iso}} \sim 3.7$  MHz) are derived for  $[\text{VO}(\text{ox})_2(\text{H}_2\text{O})]^{2-}$  with NMRD, while for  $[\text{VO}(\text{acac})(\text{H}_2\text{O})]$  a lower  ${}^1\text{H}_{\text{iso}} \sim 1.7$  MHz was obtained. The hyperfine coupling constants obtained from NMRD measurements for  $[\text{VO}(\text{ox})_2(\text{H}_2\text{O})]^{2-}$  are in good agreement with those obtained with DFT (Table 3). The known angular dependence of  ${}^1\text{H}_{\text{iso}}$ <sup>31</sup> becomes evident by comparing the values calculated for the  $[\text{VO}(\text{oxa})_2(\text{H}_2\text{O})]^{2-}$  and  $[\text{VO}(\text{oxa})_2(\text{H}_2\text{O})]^{2-}\cdot 2\text{H}_2\text{O}$  systems (Table 3). Indeed, the  $[\text{VO}(\text{oxa})_2(\text{H}_2\text{O})]^{2-}\cdot 2\text{H}_2\text{O}$  system presents a shorter  $\text{V}-\text{O}_{\text{H}_2\text{O}}$  distance than  $[\text{VO}(\text{oxa})_2(\text{H}_2\text{O})]^{2-}$  associated with a lower  ${}^1\text{H}_{\text{iso}}$  value (Table 3). Inspection of the spin density calculated for the  $[\text{VO}(\text{oxa})_2(\text{H}_2\text{O})]^{2-}$  system (Fig. 7a) shows that the positive spin density mostly resides close to the V atom, with a spatial distribution that resembles a  $d_{xy}$  orbital, as would be expected.<sup>70</sup> The vanadyl oxo atom displays a negative spin density due to spin polarization, as well as the donor

atoms of the metal coordination environment, although to a lesser extent. This is in agreement with the DFT and ENDOR studies performed in the  ${}^{17}\text{O}$  enriched  $[\text{VO}(\text{H}_2\text{O})_5]^{2+}$  system.<sup>71</sup> Spin transfer to the protons of coordinated water molecules involves the overlap of the metal  $d_{xy}$  orbital, hosting the unpaired electron, with the molecular orbitals on the hydrogen atoms of  $\text{H}_2\text{O}$ . This interaction is maximized when the H atoms lie on the  $xy$  plane leading to a large  ${}^1\text{H}_{\text{iso}}$  value.<sup>72</sup> As the protons of the water molecule are rotated out of the equatorial plane the overlap with the proton molecular orbitals is negligible and  ${}^1\text{H}_{\text{iso}}$  becomes smaller. With this in mind, the  $[\text{VO}(\text{oxa})_2(\text{H}_2\text{O})]^{2-}$  system was therefore further explored by running relaxed potential energy surface scans, in which the dihedral angle  $\phi$  defined by the  $\text{V}=\text{O}$  group and the water molecule ( $\text{O}=\text{V}-\text{O}-\text{H}$ ) was varied in the range from  $-180^\circ$  to  $+180^\circ$  (Fig. 7b). The calculated  ${}^1\text{H}_{\text{iso}}$  values are positive regardless of the value of  $\phi$ , but show two well-defined maxima at  $\phi = -90^\circ$  and  $90^\circ$ , which correspond to the situations in which the H atom of the coordinated water molecule lies on the equatorial plane. The different height of the two maxima observed for  ${}^1\text{H}_{\text{iso}}$  is related to the variations of the  $\text{V}-\text{OH}_2$  distance during the relaxed potential energy surface scan, which changes in the range  $\sim 2.18$ – $2.22$  Å. In contrast,  ${}^1\text{H}_{\text{iso}}$  reaches the minimum values when the water O–H bond is perpendicular to the equatorial plane ( $\phi = 0, 180^\circ$ ). The  ${}^1\text{H}_{\text{iso}}$  values obtained by averaging those obtained for the two  ${}^1\text{H}$  nuclei of the coordinated water molecule were found to vary in the range  $2.82$ – $1.5$  MHz, highlighting also in this case the impact of the orientation of the water molecule with respect to the  $xy$  molecular plane on the observed  ${}^1\text{H}_{\text{iso}}$ .

The angular dependence shown in Fig. 7b was previously reported for  $[\text{VO}(\text{H}_2\text{O})_5]^{2+}$ , although in the latter case negative  ${}^1\text{H}_{\text{iso}}$  values were calculated for  $\phi$  values close to  $0, 180$  and  $360^\circ$ . In the present case, DLPNO-CCSD calculations provided a small positive  ${}^1\text{H}_{\text{iso}}$  value (0.14 MHz) for  $\phi = 175^\circ$ , which supports the results obtained with DFT. We also note that DLPNO-CCSD calculations provide significantly lower  ${}^1\text{H}_{\text{iso}}$  values than DFT (the maximum value is  $\sim 1.5$  MHz), a situation that was observed earlier. In the present case DFT appears to provide  ${}^1\text{H}_{\text{iso}}$  values in better agreement with the experiment than DLPNO-CCSD. This is very likely related to the overestimation of the  $\text{V}-\text{OH}_2$  distances by DFT, as evidenced by inspecting Table 3. This effect is alleviated only in part by incorporating a few explicit second-sphere water molecules, as observed previously for other metal complexes.<sup>51,52</sup>

The experimental  ${}^1\text{H}_{\text{iso}}$  value obtained for  $[\text{VO}(\text{acac})(\text{H}_2\text{O})]$  ( ${}^1\text{H}_{\text{iso}} \sim 1.8$  MHz) is much larger than that calculated for the dominant *trans* isomer ( $\sim 0.06$  MHz). Thus, it is likely that the value of  ${}^1\text{H}_{\text{iso}}$  obtained from NMRD is related to the presence of a minor fraction of the *cis* isomer in solution. DFT calculations afford  ${}^1\text{H}_{\text{iso}}$  values of  $0.47$  MHz and  $3.27$  MHz for the *cis* isomer using the  $[\text{VO}(\text{acac})(\text{H}_2\text{O})]$  and  $[\text{VO}(\text{acac})(\text{H}_2\text{O})]\cdot 2\text{H}_2\text{O}$  systems, respectively. It is important to note that the values obtained by NMRD reflect an average of the different structures present in solution. Considering the sharp

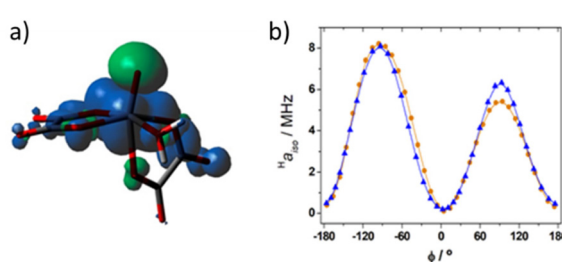


**Fig. 7** Spin density distribution in  $[\text{VO}(\text{oxa})_2(\text{H}_2\text{O})]^{2-}$  calculated at the TPSSh/Def2-TZVPP level. (a) Isosurface of the spin density corresponding to  $0.0004$  au (positive values in blue). (b)  ${}^1\text{H}_{\text{iso}}$  values calculated for the  ${}^1\text{H}$  nuclei of the coordinated water molecule as a function of  $\phi$  (see the text). The different height of the two maxima is associated with slightly different  $\text{V}-\text{OH}_2$  distances.



dependence of  $^{\text{H}}a_{\text{iso}}$  with the orientation of the water molecule, it is likely that dynamic effects play an important role.

### Rotational dynamics

The  $\tau_{\text{R}}^{298}$  value obtained from the NMRD fitting for  $[\text{VO}(\text{H}_2\text{O})_5]^{2+}$  is in excellent agreement with that estimated with EPR measurements (47.8 ps). The  $\tau_{\text{R}}^{298}$  values obtained for  $[\text{VO}(\text{ox})_2(\text{H}_2\text{O})]^{2-}$  by NMRD (52 ps) and EPR (38 ps) are also in reasonable agreement. A more significant discrepancy is however observed for  $[\text{VO}(\text{acac})(\text{H}_2\text{O})]$ , as the EPR value (77 ps) is about twice the value obtained with NMRD (30.9 ps). This discrepancy could arise from the rather large number of parameters that affect the relaxivity data, which introduces some uncertainties in the values of some of them. Nevertheless, we also stress that the  $\tau_{\text{R}}^{298}$  values obtained by NMRD refer to the reorientation of the V...H vector involving the coordinated water molecule, while the  $\tau_{\text{R}}^{298}$  values obtained by EPR likely reflect better the rotation of the whole molecule. For instance, the local mobility of the water molecule coordinated to  $\text{Gd}^{3+}$  results in shorter  $\tau_{\text{R}}^{298}$  values for the V...H vector than the V...O one, with  $\tau_{\text{RH}}^{298}/\tau_{\text{RO}}^{298} \sim 0.65$ .<sup>73</sup> In contrast, intramolecular hydrogen bonding interactions involving the coordinated water molecule may restrict local rotation, resulting in an enhanced relaxivity.<sup>74</sup>

### Electron relaxation

The fitting of the NMRD data yields similar values for the electron relaxation time  $T_1^{\text{e}}$ , which are around 1 ns (Table 4). However, we have made a number of assumptions during the fitting, and thus these results should be obtained with some care. Indeed, we assumed that  $T_1^{\text{e}}$  does not change with the applied magnetic field, and further that  $T_1^{\text{e}} = T_2^{\text{e}}$ . Electronic relaxation in  $d^1$  complexes is likely the result of the time modulation of the  $g$ - and  $A$ -tensors,<sup>16</sup> probably as a result of rotation and fluctuations of the metal coordination sphere caused by molecular vibrations and collisions with the solvent. For some of the complexes good fits of the data were only possible by assuming the  $T_1^{\text{e}}$  changes with temperature following Arrhenius behaviour with an activation energy  $E_s$  (Table 4). We note that the  $[\text{VO}(\text{nta})(\text{H}_2\text{O})]^-$  and  $[\text{VO}(\text{acac})(\text{H}_2\text{O})]$  complexes show shorter  $T_1^{\text{e}}$  values than the remaining complexes studied here, which is in qualitative agreement with the EPR relaxation data discussed above (Fig. 5). However, further experimental and theoretical studies are necessary to gain a better understanding of electron relaxation in the aqueous solutions of oxovanadium(IV) complexes.

### Water exchange

The  $\tau_{\text{M}}^{298}$  for the vanadyl aqua-ion is sensibly longer compared to the values observed for  $[\text{Gd}(\text{H}_2\text{O})_8]^{3+}$  ( $\tau_{\text{M}}^{298} = 1.2$  ns)<sup>37</sup> and  $[\text{Mn}(\text{H}_2\text{O})_6]^{3+}$  ( $\tau_{\text{M}}^{298} = 35.5$  ns).<sup>38</sup> The  $\tau_{\text{M}}^{298}$  value of 19.1  $\mu\text{s}$  is also sensibly shorter than that determined for the equatorial water molecules using  $^{17}\text{O}$  NMR measurements (2 ms).<sup>75</sup> This suggests that  $^1\text{H}$  exchange is faster than the exchange of the whole water molecule due to the prototropic contribution to water exchange at the acidic pH used for NMRD measure-

ments. A similar effect was reported recently for  $[\text{Fe}(\text{H}_2\text{O})_6]^{3+}$ , which is characterized by a  $\tau_{\text{MO}}^{298}$  value of the whole water of 25  $\mu\text{s}$ , and a  $\tau_{\text{MH}}^{298}$  value of 756 ns in 0.15 M  $\text{HNO}_3$ .<sup>39</sup>

The  $[\text{VO}(\text{oxa})_2(\text{H}_2\text{O})]^{2-}$  and  $[\text{VO}(\text{nta})(\text{H}_2\text{O})]^-$  complexes show similar residence times of the coordinated water molecule ( $\sim 15$   $\mu\text{s}$ , Table 4), while for  $[\text{VO}(\text{acac})_2(\text{H}_2\text{O})]$  water exchange is faster. The related activation enthalpy ( $\Delta H^\ddagger$ ) assumes similar values for all complexes except  $[\text{VO}(\text{oxa})_2(\text{H}_2\text{O})]^{2-}$ . The very high enthalpy barrier determined for the latter may be related to the expulsion of the coordinated water molecule from the inner-coordination sphere as a result of interconversion between the *cis* and *trans* isomers. This process would shift the coordinated water molecule to the labile *trans* position, facilitating water exchange. Support for this hypothesis is provided by the detection of a minor fraction of the *trans* isomer in solution using EPR measurements (4%).<sup>76</sup> An  $^1\text{H}$  exchange mechanism involving the rearrangement of the water ligand from an equatorial to an axial position was suggested previously on the grounds of a  $T_2^{\text{H}}$  NMR relaxation study. The same work reported an  $^1\text{H}$   $\tau_{\text{M}}^{298}$  value for  $[\text{VO}(\text{oxa})_2(\text{H}_2\text{O})]^{2-}$  (5.4  $\mu\text{s}$ ) somewhat longer than that determined here. Most likely water exchange in  $[\text{VO}(\text{acac})_2(\text{H}_2\text{O})]$  also involves interconversion between the *cis* and *anti* isomers, which are both present in solution. This explains the presence of a scalar contribution to relaxivity associated with a rather large  $^{\text{H}}a_{\text{iso}}$  value, which is not expected for the major *trans* isomer.

### Conclusions

We have reported an integrated EPR,  $^1\text{H}$  relaxometric and computational study that provides very detailed information on the magnetic and dynamic properties of oxovanadium(IV) complexes in solution. The structure of the complexes in aqueous solution was established by using a combination of EPR and computational studies. This allowed estimating different parameters that affect the  $^1\text{H}$  relaxation times of the solutions of these complexes in water, including the distances of the closest approach of second-sphere water molecules, the distance between the  $^1\text{H}$  nuclei of coordinated water molecules and the paramagnetic centre and rotational correlation times. The inner-sphere contribution to  $^1\text{H}$  relaxivities was found to display contributions from both the scalar and dipolar mechanisms. Water exchange in this series of complexes occurs in the  $\mu\text{s}$  timescale, with all complexes showing similar water exchange rates. The  $^{\text{H}}a_{\text{iso}}$  values obtained from NMRD were corroborated with DFT calculations, which show that the orientation of the coordinated water molecule affects dramatically the hyperfine coupling constant.

The details on the magnetic and relaxation properties of oxovanadium(IV) complexes revealed here are relevant for the development of molecular probes for different applications, including molecular spin qubits and MRI contrast agents.

More generally, we believe that this methodology, which synergistically combines two complementary spectroscopic



techniques and computational procedures, represents a significant advance in the characterization of paramagnetic species in solution. Compared to the traditional approach based on the measurement and analysis of data collected with a single experimental technique, this methodology provides a more complete, accurate and reliable set of structural and dynamic information.

## Experimental section

### Sample preparation

All the precursors were high purity reagents from Sigma Aldrich. The  $[\text{VO}(\text{H}_2\text{O})_5]^{2+}$  complex was obtained by dissolving 8 mg of  $\text{VOSO}_4$  in 10 mL of water at  $\text{pH} < 2$ , adjusted with  $\text{H}_2\text{SO}_4$ . For  $[\text{VO}(\text{oxa})_2(\text{H}_2\text{O})]^{2-}$  (ref. 67 and 76) and  $[\text{VO}(\text{nta})(\text{H}_2\text{O})]^-$  (ref. 66 and 77) complexes the procedure was similar, using a nearly 1 : 1 molar ratio between the metal ion and the ligand in solution. 3 mg of nitrilotriacetic acid, or 3 mg of oxalic acid, were dissolved in 3 mL of water, and then the pH was adjusted to about 5–6 pH units with a NaOH solution and 2.5 mg of  $\text{VOSO}_4$  were added to the solution. For the  $[\text{VO}(\text{dtpa})]^{3-}$  complex (1 : 1 molar ratio), 10 mg of the ligand were dissolved in 2.5 mL of water containing 5 mg of  $\text{VOSO}_4$ , the mixture was stirred for 1 hour and then the pH was adjusted to 7 with a 5% of  $\text{NaHCO}_3$  solution.<sup>15</sup> The  $[\text{VO}(\text{acac})_2]$  complex was prepared according to literature protocols.<sup>78</sup>  $\text{V}_2\text{O}_5$  was dissolved in a 3 : 2  $\text{H}_2\text{O} : \text{H}_2\text{SO}_4$  (conc) solution. Then 5 mL of ethanol were added, and the resulting solution was heated at reflux temperature under stirring for 1 hour. Excess  $\text{V}_2\text{O}_5$  was removed by filtration and acetylacetone was added under stirring at  $\text{pH} = 7$ . The concentration of the complexes in solution is tested with the Evans method,<sup>79</sup> which afforded the following values:  $[\text{VO}(\text{H}_2\text{O})_5]^{2+} = 3.5 \text{ mM}$ ,  $[\text{VO}(\text{dtpa})]^{3-} = 1.8 \text{ mM}$ ,  $[\text{VO}(\text{oxa})_2(\text{H}_2\text{O})]^{2-} = 3.9 \text{ mM}$ ,  $[\text{VO}(\text{nta})(\text{H}_2\text{O})]^- = 12.2 \text{ mM}$  and  $[\text{VO}(\text{acac})_2] = 14.1 \text{ mM}$ . For pulse EPR measures the latter two solutions were diluted to  $\sim 3 \text{ mM}$  in order to have similar concentrations for all complexes.

### <sup>1</sup>H NMRD measurements

The  $1/T_1^{\text{H}}$  <sup>1</sup>H Nuclear Magnetic Relaxation Dispersion (NMRD) profiles were measured on a Fast-Field Cycling (FFC) Stelar SmarTracer Relaxometer over a continuum of magnetic field strengths from 0.00024 to 0.25 T (corresponding to 0.01–10 MHz proton Larmor frequencies). The relaxometer operates under computer control with an absolute uncertainty in  $1/T_1^{\text{H}}$  of  $\pm 1\%$ . Additional data points in the range 20–120 MHz were obtained with a High Field Relaxometer (Stelar) equipped with the HTS-110 3T Metrology Cryogen-free Superconducting Magnet. The measurements were performed using the standard inversion recovery sequence (20 experiments, 2 scans) with a typical 90° pulse width of 3.5  $\mu\text{s}$  and the reproducibility of the data was within  $\pm 0.5\%$ . The temperature was controlled with a Stelar VTC-91 heater airflow equipped with a copper-constantan thermocouple (uncertainty of  $\pm 0.1 \text{ K}$ ).

### EPR measurements

X-band CW-EPR spectra were recorded on a Bruker EMX spectrometer (MW frequency 9.75 GHz) equipped with a cylindrical cavity. Q-band pulse EPR and Q-band CW EPR experiments were performed on a Bruker ELEXSYS E580 spectrometer (MW frequency 9.76 GHz and 34 GHz respectively) equipped with a continuous helium flow cryostat from Oxford Inc. The magnetic field was measured by means of a Bruker ER035M NMR gaussmeter. Electron-Spin-Echo (ESE)-detected EPR experiments were carried out with the pulse sequence  $\pi/2-\tau-\pi-\tau$ -echo. The microwave pulse lengths  $t_{\pi/2}$  and  $t_{\pi}$  and the  $\tau$  value employed are specified in the corresponding figure captions.  $T_m^e$  measurements were performed using a two-pulse Hahn spin echo sequence,  $\pi/2-\tau-\pi-\tau$ -echo and varying the inter-pulse delay  $\tau$  from an initial value of 120 ns with time increments of 8 ns for 800 points. The  $\pi/2$  and  $\pi$  lengths were set to 16 and 32 ns, respectively.  $T_1^e$  measurements were performed through the inversion recovery pulse sequence,  $\pi-T-\pi/2-\tau-\pi-\tau$ -echo, where the interpulse delay  $T$  has an initial value of  $1 \times 10^5 \text{ ns}$ ,  $\pi/2$  and  $\pi$  have a length 16 and 32 ns, respectively, and  $\tau$  is fixed to 400 ns. The time increments of  $T$  and the shot-repetition rate were adjusted at each temperature. For low temperature measurements 30% glycerol solutions were prepared in order to obtain good low  $T$  glasses.

### Computational details

Geometry optimizations of the vanadium(IV) complexes were performed with the Gaussian 16 program package (Rev B.01)<sup>80</sup> using unrestricted Kohn-Sham calculations with the hybrid-meta GGA functional TPSSh<sup>56</sup> and the Def2-TZVPP<sup>81</sup> basis set. Solvent effects were incorporated with a polarized continuum model<sup>82</sup> using the default settings [scrf = (pcm, solvent = water)]. The integration grid was increased using the integral = superfinegrid keyword. Frequency calculations were used to confirm that the optimized structures corresponded to stationary points.

The computation of  $A$ - and  $g$ -tensors was carried out using the ORCA program system (release 5.0.3).<sup>83,84</sup> The  $A$ -tensors were computed with both the TPSSh and TPSS0 functionals,<sup>55</sup> and the Def2-QZVPP basis set.<sup>81</sup> The TPSS0 functional is a 25% exchange version of TPSSh. The  $g$ -tensors were computed with the  $N$ -electron valence perturbation theory to second order (SC-NEVPT2)<sup>85</sup> on the basis of complete active space self-consisted field (CASSCF)<sup>86</sup> calculations. The active space consisted of one electron distributed in five metal based 3d orbitals [CAS(1,5)]. All calculations were performed with the aid of the resolution of identity (RI) approximation for both Coulomb and exchange (RI-JK)<sup>87</sup> using the Def2/JK<sup>88</sup> auxiliary basis set. The second order contribution to the  $A$ -tensor from spin orbit coupling was considered with the spin-orbit mean-field method [SOMF(1X)].<sup>89</sup> The integration grids were increased from the defaults using the AngularGrid 7 and IntAcc 5.0 options within the %method section. The quality of the  $A$ -tensors obtained with DFT was tested using the coupled cluster theory, including single and double excitations, with



the domain based local pair natural orbital method (DLPNO-CCSD).<sup>90,91</sup> These calculations used the default settings defined by the DLPNO-HFC1 keyword.<sup>59</sup> Bulk water solvent effects in all ORCA calculations were introduced with the SMD model developed by Truhlar,<sup>92</sup> which is based on the electron density of the solute and a polarized continuum.

## Author contributions

V. L.: EPR data and NMRD profiles. F. C.: synthesis, purification, and characterization of the complexes, and NMRD profiles. D. E.-G.: DFT calculations. C. P.-I.: DFT calculations, NMR data analysis, conceptualization and manuscript preparation. M. C.: EPR studies, data analysis, conceptualization and manuscript preparation. M. B.: project supervision, conceptualization and manuscript preparation.

## Conflicts of interest

There are no conflicts to declare.

## Acknowledgements

M. B. and F. C. acknowledge the financial support from the Ministero dell'Università e della Ricerca (PRIN 2017A2KEPL project). C. P.-I. and D. E. G. thank Ministerio de Ciencia e Innovación (PID2019-104626GB-I00) and Xunta de Galicia (Grant ED431B 2020/52) for generous financial support, and acknowledge Centro de Supercomputación de Galicia for providing access to computing facilities.

## References

- 1 M. C. Heffern, L. M. Matosziuk and T. J. Meade, Lanthanide probes for bioresponsive imaging, *Chem. Rev.*, 2014, **114**, 4496–4539.
- 2 J. Wahsner, E. M. Gale, A. Rodríguez-Rodríguez and P. Caravan, Chemistry of MRI Contrast Agents: Current Challenges and New Frontiers, *Chem. Rev.*, 2019, **119**, 957–1057.
- 3 G. Angelovski and É. Tóth, Strategies for sensing neurotransmitters with responsive MRI contrast agents, *Chem. Soc. Rev.*, 2017, **46**, 324–336.
- 4 F. Troiani and M. Affronte, Molecular spins for quantum information technologies, *Chem. Soc. Rev.*, 2011, **40**, 3119.
- 5 M. Atzori and R. Sessoli, The Second Quantum Revolution: Role and Challenges of Molecular Chemistry, *J. Am. Chem. Soc.*, 2019, **141**, 11339–11352.
- 6 J. M. Zadrozny, J. Niklas, O. G. Poluektov and D. E. Freedman, Millisecond Coherence Time in a Tunable Molecular Electronic Spin Qubit, *ACS Cent. Sci.*, 2015, **1**, 488–492.
- 7 L. Helm, Relaxivity in paramagnetic systems: Theory and mechanisms, *Prog. Nucl. Magn. Reson. Spectrosc.*, 2006, **49**, 45–64.
- 8 J. M. Zadrozny, J. Niklas, O. G. Poluektov and D. E. Freedman, Multiple Quantum Coherences from Hyperfine Transitions in a Vanadium(IV) Complex, *J. Am. Chem. Soc.*, 2014, **136**, 15841–15844.
- 9 M. Atzori, L. Tesi, E. Morra, M. Chiesa, L. Sorace and R. Sessoli, Room-Temperature Quantum Coherence and Rabi Oscillations in Vanadyl Phthalocyanine: Toward Multifunctional Molecular Spin Qubits, *J. Am. Chem. Soc.*, 2016, **138**, 2154–2157.
- 10 M. Atzori, E. Morra, L. Tesi, A. Albino, M. Chiesa, L. Sorace and R. Sessoli, Quantum Coherence Times Enhancement in Vanadium(IV)-based Potential Molecular Qubits: the Key Role of the Vanadyl Moiety, *J. Am. Chem. Soc.*, 2016, **138**, 11234–11244.
- 11 L. Tesi, E. Lucaccini, I. Cimatti, M. Perfetti, M. Mannini, M. Atzori, E. Morra, M. Chiesa, A. Caneschi, L. Sorace and R. Sessoli, Quantum coherence in a processable vanadyl complex: new tools for the search of molecular spin qubits, *Chem. Sci.*, 2016, **7**, 2074–2083.
- 12 I. Gimeno, A. Urtizberea, J. Román-Roche, D. Zueco, A. Camón, P. J. Alonso, O. Roubeau and F. Luis, Broadband spectroscopy of a vanadyl porphyrin: a model electro-nuclear spin qudit, *Chem. Sci.*, 2021, **12**, 5621–5630.
- 13 C. E. Jackson, C.-Y. Lin, S. H. Johnson, J. van Tol and J. M. Zadrozny, Nuclear-spin-pattern control of electron-spin dynamics in a series of V(IV) complexes, *Chem. Sci.*, 2019, **10**, 8447–8454.
- 14 C.-Y. Lin, T. Ngendahimana, G. R. Eaton, S. S. Eaton and J. M. Zadrozny, Counterion influence on dynamic spin properties in a V(IV) complex, *Chem. Sci.*, 2019, **10**, 548–555.
- 15 J. W. Chen, R. L. Belford and R. B. Clarkson, Second-Sphere and Outer-Sphere Proton Relaxation of Paramagnetic Complexes: From EPR to NMRD, *J. Phys. Chem. A*, 1998, **102**, 2117–2130.
- 16 I. Bertini, Z. Xia and C. Luchinat, Solvent water <sup>1</sup>H NMRD study of oxovanadium(IV) aquo ion, *J. Magn. Reson.*, 1992, **99**, 235–246.
- 17 D. Mustafi, B. Peng, S. Foxley, M. W. Makinen, G. S. Karczmar, M. Zamora, J. Ejnik and H. Martin, New vanadium-based magnetic resonance imaging probes: Clinical potential for early detection of cancer, *JBIC, J. Biol. Inorg. Chem.*, 2009, **14**, 1187–1197.
- 18 D. Rehder, The potentiality of vanadium in medicinal applications, *Inorg. Chim. Acta*, 2020, **504**, 119445.
- 19 E. Anoardo, G. Galli and G. Ferrante, Fast-field-cycling NMR: Applications and instrumentation, *Appl. Magn. Reson.*, 2001, **20**, 365–404.
- 20 S. Aime, M. Botta, D. Esteban-Gómez and C. Platas-Iglesias, Characterisation of magnetic resonance imaging (MRI) contrast agents using NMR relaxometry, *Mol. Phys.*, 2019, **117**, 898–909.
- 21 J. H. Freed, Dynamic effects of pair correlation functions on spin relaxation by translational diffusion in liquids. II.



Finite jumps and independent  $T_1$  processes, *J. Chem. Phys.*, 1978, **68**, 4034–4037.

22 P. H. Fries, C. Gateau and M. Mazzanti, Practical Route to Relative Diffusion Coefficients and Electronic Relaxation Rates of Paramagnetic Metal Complexes in Solution by Model-Independent Outer-Sphere NMRD. Potentiality for MRI Contrast Agents, *J. Am. Chem. Soc.*, 2005, **127**, 15801–15814.

23 J. A. Peters, The reliability of parameters obtained by fitting of  $^1\text{H}$  NMRD profiles and  $^{17}\text{O}$  NMR data of potential  $\text{Gd}^{3+}$ -based MRI contrast agents, *Contrast Media Mol. Imaging*, 2016, **11**, 160–168.

24 N. F. Albanese and N. D. Chasteen, Origin of the electron paramagnetic resonance line widths in frozen solution of the oxovanadium(IV) ion, *J. Phys. Chem.*, 1978, **82**, 910–914.

25 I. E. Haedicke, T. Li, Y. L. K. Zhu, F. Martinez, A. M. Hamilton, D. H. Murrell, J. T. Nofiele, H.-L. M. Cheng, T. J. Scholl, P. J. Foster and X. Zhang, An enzyme-activatable and cell-permeable  $\text{Mn}^{\text{III}}$ -porphyrin as a highly efficient  $T_1$  MRI contrast agent for cell labeling, *Chem. Sci.*, 2016, **7**, 4308–4317.

26 S. Stoll and A. Schweiger, EasySpin, a comprehensive software package for spectral simulation and analysis in EPR, *J. Magn. Reson.*, 2006, **178**, 42–55.

27 Y. Zhou, B. E. Bowler, G. R. Eaton and S. S. Eaton, Electron spin lattice relaxation rates for S=12 molecular species in glassy matrices or magnetically dilute solids at temperatures between 10 and 300 K, *J. Magn. Reson.*, 1999, **139**, 165–174.

28 G. R. Eaton and S. S. Eaton, Solvent and temperature dependence of spin echo dephasing for chromium(V) and vanadyl complexes in glassy solution, *J. Magn. Reson.*, 1999, **136**, 63–68.

29 T. S. Smith, R. LoBrutto and V. L. Pecoraro, Paramagnetic spectroscopy of vanadyl complexes and its applications to biological systems, *Coord. Chem. Rev.*, 2002, **228**, 1–18.

30 C. F. Mulks, B. Kirste and H. Van Willigen, ENDOR Study of  $\text{V}^{2+}$ -imidazole Complexes in Frozen Aqueous Solution, *J. Am. Chem. Soc.*, 1982, **104**, 5906–5911.

31 A. C. Saladino and S. C. Larsen, Density Functional Theory Calculations of the Electron Paramagnetic Resonance Parameters for  $\text{VO}^{2+}$  Complexes, *J. Phys. Chem. A*, 2003, **107**, 1872–1878.

32 S. S. Amin, K. Cryer, B. Zhang, S. K. Dutta, S. S. Eaton, O. P. Anderson, S. M. Miller, B. A. Reul, S. M. Brichard and D. C. Crans, Chemistry and Insulin-Mimetic Properties of Bis(acetylacetone)oxovanadium(IV) and Derivatives, *Inorg. Chem.*, 2000, **39**, 406–416.

33 R. E. Oughtred, E. S. Raper and H. M. M. Shearer, The crystal structure of diammonium bis(oxalato)monoaquaoxovanadate(IV) monohydrate, *Acta Crystallogr., Sect. B: Struct. Crystallogr. Cryst. Chem.*, 1976, **32**, 82–87.

34 A. Tesmar, I. Inklewicz-Stepniak, A. Sikorski, D. Wyrzykowski, D. Jacewicz, P. Zięba, J. Pranczak, T. Ossowski and L. Chmurzyński, Structure, physico-chemical and biological properties of new complex salt of aqua-(nitrilotriacetato-N,O,O',O")-oxidovanadium(IV) anion with 1,10-phenanthrolinium cation, *J. Inorg. Biochem.*, 2015, **152**, 53–61.

35 A. Tesmar, D. Wyrzykowski, K. Kazimierczuk, J. Kłak, S. Kowalski, I. Inklewicz-Stepniak, J. Drzeżdżon, D. Jacewicz and L. Chmurzyński, Structure, Physicochemical and Biological Properties of an Aqua (2,2',2"-Nitrilotriacetato)-oxidovanadium(IV) Salt with 4-Methylpyridinium Cation, *Z. Anorg. Allg. Chem.*, 2017, **643**, 501–510.

36 A. B. Ilyukhin, L. M. Shkol'nikova, A. L. Poznyak and S. S. Makarevich, Crystal structure of diethylenetriaminepentaacetato(2-)vanadyl monohydrate, *Koord. Khim.*, 1991, **17**, 918–921.

37 D. H. Powell, O. M. N. Dhubhghaill, D. Pubanz, L. Helm, Y. S. Lebedev, W. Schlaepfer and A. E. Merbach, Structural and Dynamic Parameters Obtained from  $^{17}\text{O}$  NMR, EPR, and NMRD Studies of Monomeric and Dimeric  $\text{Gd}^{3+}$  Complexes of Interest in Magnetic Resonance Imaging: An Integrated and Theoretically Self-Consistent Approach, *J. Am. Chem. Soc.*, 1996, **118**, 9333–9346.

38 D. Esteban-Gómez, C. Cassino, M. Botta and C. Platas-Iglesias,  $^{17}\text{O}$  and  $^1\text{H}$  relaxometric and DFT study of hyperfine coupling constants in  $[\text{Mn}(\text{H}_2\text{O})_6]^{2+}$ , *RSC Adv.*, 2014, **4**, 7094.

39 Z. Baranyai, F. Carniato, A. Nucera, D. Horváth, L. Tei, C. Platas-Iglesias and M. Botta, Defining the conditions for the development of the emerging class of  $\text{Fe}^{\text{III}}$ -based MRI contrast agents, *Chem. Sci.*, 2021, **12**, 11138–11145.

40 M. Atzori, S. Benci, E. Morra, L. Tesi, M. Chiesa, R. Torre, L. Sorace and R. Sessoli, Structural Effects on the Spin Dynamics of Potential Molecular Qubits, *Inorg. Chem.*, 2018, **57**, 731–740.

41 J.-L. Du, G. R. Eaton and S. S. Eaton, Electron Spin Relaxation in Vanadyl, Copper(II), and Silver(II) Porphyrins in Glassy Solvents and Doped Solids, *J. Magn. Reson., Ser. A*, 1996, **119**, 240–246.

42 E. Balogh, Z. He, W. Hsieh, S. Liu and É. Tóth, Dinuclear Complexes Formed with the Triazacyclononane Derivative ENOTA $^{4-}$ : High-Pressure  $^{17}\text{O}$  NMR Evidence of an Associative Water Exchange on  $[\text{Mn}_2^{\text{II}}(\text{ENOTA})(\text{H}_2\text{O})_2]$ , *Inorg. Chem.*, 2007, **46**, 238–250.

43 I. Bertini, F. Briganti, Z. Xia and C. Luchinat, Nuclear Magnetic Relaxation Dispersion Studies of Hexaaquo Mn(II) Ions in Water-Glycerol Mixtures, *J. Magn. Reson., Ser. A*, 1993, **101**, 198–201.

44 M. Magnussen, T. Brock-Nannestad and J. Bendix, Penta-aqua-oxovanadium(IV) bis(trifluoro-methane-sulfonate), *Acta Crystallogr., Sect. C: Cryst. Struct. Commun.*, 2007, **63**, m51–m53.

45 A. Tézé, C. Marchal-Roch, H. So, M. Fournier and G. Hervé, Synthesis, X-ray crystal structure, and EPR study of  $[\text{Na}(\text{H}_2\text{O})_2]_2[\text{VO}(\text{H}_2\text{O})_5][\text{SiW}_{12}\text{O}_{40}] \cdot 4\text{H}_2\text{O}$ , *Solid State Sci.*, 2001, **3**, 329–338.

46 J. Krakowiak, D. Lundberg and I. Persson, A Coordination Chemistry Study of Hydrated and Solvated Cationic



Vanadium Ions in Oxidation States +III, +IV, and +V in Solution and Solid State, *Inorg. Chem.*, 2012, **51**, 9598–9609.

47 L. Lin, S. Wu, C. Huang, H. Zhang, X. Huang and Z. Lian, Piperazinium aqua-bis-(oxalato)-oxovanadate(IV) sesquihydrate, *Acta Crystallogr., Sect. E: Struct. Rep. Online*, 2004, **60**, m631–m633.

48 H. Sehimi, I. Chérif and M. F. Zid, Crystal structure of bis-[4-(di-methyl-amino)-pyridinium]aqua-bis-(oxalato)oxidovanadate(IV) dihydrate, *Acta Crystallogr., Sect. E: Crystallogr. Commun.*, 2016, **72**, 1002–1005.

49 N. M. Atherton and J. F. Shackleton, Proton ENDOR of  $\text{VO}^{2+}$  in  $\text{Mg}(\text{NH}_4)_2(\text{SO}_4)_2 \cdot 6\text{H}_2\text{O}$ , *Mol. Phys.*, 1980, **39**, 1471–1485.

50 R. B. P. Pesci, E. J. de Souza, E. Niquet, O. R. Nascimento, R. B. Viana and V. M. Deflon, Supramolecular structures in oxovanadium(IV) compounds with pyrid-2-one and pyrid-4-one ligands, *J. Mol. Struct.*, 2019, **1194**, 104–111.

51 D. Esteban-Gómez, A. de Blas, T. Rodríguez-Blas, L. Helm and C. Platas-Iglesias, Hyperfine Coupling Constants on Inner-Sphere Water Molecules of GdIII-Based MRI Contrast Agents, *ChemPhysChem*, 2012, **13**, 3640–3650.

52 V. Patinec, G. A. Rolla, M. Botta, R. Tripier, D. Esteban-Gómez and C. Platas-Iglesias, Hyperfine Coupling Constants on Inner-Sphere Water Molecules of a Triazacyclononane-based Mn(II) Complex and Related Systems Relevant as MRI Contrast Agents, *Inorg. Chem.*, 2013, **52**, 11173–11184.

53 V. Nagarajan, B. Müller, O. Storcheva, K. Köhler and A. Pöpll, Coordination of solvent molecules to  $\text{VO}(\text{acac})_2$  complexes in solution studied by hyperfine sublevel correlation spectroscopy and pulsed electron nuclear double resonance, *Res. Chem. Intermed.*, 2007, **33**, 705–724.

54 G. Anderegg, F. Arnaud-Neu, R. Delgado, J. Felcman and K. Popov, Critical evaluation of stability constants of metal complexes of complexones for biomedical and environmental applications\* (IUPAC Technical Report), *Pure Appl. Chem.*, 2005, **77**, 1445–1495.

55 S. Grimme, Accurate Calculation of the Heats of Formation for Large Main Group Compounds with Spin-Component Scaled MP2 Methods, *J. Phys. Chem. A*, 2005, **109**, 3067–3077.

56 J. Tao, J. P. Perdew, V. N. Staroverov and G. E. Scuseria, Climbing the Density Functional Ladder: Nonempirical Meta-Generalized Gradient Approximation Designed for Molecules and Solids, *Phys. Rev. Lett.*, 2003, **91**, 146401.

57 D. Sanna, G. Sciortino, V. Ugone, G. Micera and E. Garribba, Nonoxido  $\text{V}^{IV}$  Complexes: Prediction of the EPR Spectrum and Electronic Structure of Simple Coordination Compounds and Amavadin, *Inorg. Chem.*, 2016, **55**, 7373–7387.

58 O. I. Gromov, Performance of the DLPNO-CCSD and recent DFT methods in the calculation of isotropic and dipolar contributions to 14N hyperfine coupling constants of nitroxide radicals, *J. Mol. Model.*, 2021, **27**, 194.

59 M. Saitow and F. Neese, Accurate spin-densities based on the domain-based local pair-natural orbital coupled-cluster theory, *J. Chem. Phys.*, 2018, **149**, 034104.

60 G. Micera and E. Garribba, Is the spin-orbit coupling important in the prediction of the  $^{51}\text{V}$  hyperfine coupling constants of  $\text{V}^{IV}\text{O}^{2+}$  species? ORCA versus Gaussian performance and biological applications, *J. Comput. Chem.*, 2011, 2822–2835.

61 S. P. de Visser, M. G. Quesne, B. Martin, P. Comba and U. Ryde, Computational modelling of oxygenation processes in enzymes and biomimetic model complexes, *Chem. Commun.*, 2014, **50**, 262–282.

62 E. Lelong, J.-M. Suh, G. Kim, D. Esteban-Gómez, M. Cordier, M. H. Lim, R. Delgado, G. Royal, C. Platas-Iglesias, H. Bernard and R. Tripier, Complexation of C-Functionalized Cyclams with Copper(II) and Zinc(II): Similarities and Changes When Compared to Parent Cyclam Analogues, *Inorg. Chem.*, 2021, **60**, 10857–10872.

63 S. Maurelli, G. Berlier, M. Chiesa, F. Musso and F. Corà, Structure of the catalytic active sites in vanadium-doped aluminophosphate microporous materials. New evidence from spin density studies, *J. Phys. Chem. C*, 2014, **118**, 19879–19888.

64 R. C. R. Bottini, L. G. Fachini, G. B. Baptistella, D. Stinghen, F. S. Santana, M. Briganti, R. R. Ribeiro, J. F. Soares, E. L. Sá and G. G. Nunes, An unsymmetrical mixed-valence oxidovanadium(IV/V) binuclear complex: Synthesis, characterization, DFT studies, and bromoperoxidase activity, *Inorg. Chim. Acta*, 2022, **537**, 120947.

65 L. Vander Elst, A. Sessoye, S. Laurent and R. N. Muller, Can the Theoretical Fitting of the Proton-Nuclear-Magnetic-Relaxation-Dispersion (Proton NMRD) Curves of Paramagnetic Complexes Be Improved by Independent Measurement of Their Self-Diffusion Coefficients?, *Helv. Chim. Acta*, 2005, **88**, 574–587.

66 G. A. Rolla, C. Platas-Iglesias, M. Botta, L. Tei and L. Helm,  $^1\text{H}$  and  $^{17}\text{O}$  NMR Relaxometric and Computational Study on Macrocyclic Mn(II) Complexes, *Inorg. Chem.*, 2013, **52**, 3268–3279.

67 R. Mills, Self-diffusion in normal and heavy water in the range 1–45.deg., *J. Phys. Chem.*, 1973, **77**, 685–688.

68 D. Mustafi and M. W. Mäkinen, Structure and Conformation of Bis(acetylacetonato)oxovanadium(IV) and Bis(maltolato)oxovanadium(IV) in Solution Determined by Electron Nuclear Double Resonance Spectroscopy, *Inorg. Chem.*, 2005, **44**, 5580–5590.

69 L. Helm and A. E. Merbach, Inorganic and bioinorganic solvent exchange mechanisms, *Chem. Rev.*, 2005, **105**, 1923–1960.

70 E. Ruiz, J. Cirera and S. Alvarez, Spin density distribution in transition metal complexes, *Coord. Chem. Rev.*, 2005, **249**, 2649–2660.

71 D. Baute and D. Goldfarb, The  $^{17}\text{O}$  Hyperfine Interaction in  $\text{V}^{IV}\text{O}(\text{H}_2^{17}\text{O})_5^{2+}$  and  $\text{Mn}(\text{H}_2^{17}\text{O})_6^{2+}$  Determined by High Field ENDOR Aided by DFT Calculations, *J. Phys. Chem. A*, 2005, **109**, 7865–7871.



72 S. C. Larsen, DFT Calculations of Proton Hyperfine Coupling Constants for  $[\text{VO}(\text{H}_2\text{O})_5]^{2+}$ : Comparison with Proton ENDOR Data, *J. Phys. Chem. A*, 2001, **105**, 8333–8338.

73 F. A. Dunand, A. Borel and A. E. Merbach, How Does Internal Motion Influence the Relaxation of the Water Protons in  $\text{Ln}^{III}$ DOTA-like Complexes?, *J. Am. Chem. Soc.*, 2002, **124**, 710–716.

74 E. Boros, R. Srinivas, H. Kim, A. M. Raitsimring, A. V. Astashkin, O. G. Poluektov, J. Niklas, A. D. Horning, B. Tidor and P. Caravan, Intramolecular Hydrogen Bonding Restricts Gd–Aqua-Ligand Dynamics, *Angew. Chem., Int. Ed.*, 2017, **56**, 5603–5606.

75 K. Wuethrich and R. E. Connick, Nuclear Magnetic Resonance Relaxation of Oxygen-17 in Aqueous Solutions of Vanadyl Perchlorate and the Rate of Elimination of Water Molecules from the First Coordination Sphere, *Inorg. Chem.*, 1967, **6**, 583–590.

76 P. Buglyó, E. Kiss, I. Fábián, T. Kiss, D. Sanna, E. Garribba and G. Micera, Speciation and NMR relaxation studies of VO(IV) complexes with several O-donor containing ligands: oxalate, malonate, maltolate and kojate, *Inorg. Chim. Acta*, 2000, **306**, 174–183.

77 D. Sanna, I. Bódi, S. Bouhsina, G. Micera and T. Kiss, Oxovanadium(IV) complexes of phosphonic derivatives of iminodiacetic and nitrilotriacetic acids, *J. Chem. Soc., Dalton Trans.*, 1999, 3275–3282.

78 R. N. Rogers and G. E. Pake, Paramagnetic Relaxation in Solutions of  $\text{VO}^{++}$ , *J. Chem. Phys.*, 1960, **33**, 1107–1111.

79 D. M. Corsi, C. Platas-Iglesias, H. van Bekkum and J. A. Peters, Determination of paramagnetic lanthanide(III) concentrations from bulk magnetic susceptibility shifts in NMR spectra., *Magn. Reson. Chem.*, 2001, **39**, 723–726.

80 M. J. Frisch, G. W. Trucks, H. B. Schlegel, G. E. Scuseria, M. A. Robb, J. R. Cheeseman, G. Scalmani, V. Barone, G. A. Petersson, H. Nakatsuji, X. Li, M. Caricato, A. V. Marenich, J. Bloino, B. G. Janesko, R. Gomperts, B. Mennucci, H. P. Hratchian, J. V. Ortiz, A. F. Izmaylov, J. L. Sonnenberg, D. Williams-Young, F. Ding, F. Lipparini, F. Egidi, J. Goings, B. Peng, A. Petrone, T. Henderson, D. Ranasinghe, V. G. Zakrzewski, J. Gao, N. Rega, G. Zheng, W. Liang, M. Hada, M. Ehara, K. Toyota, R. Fukuda, J. Hasegawa, M. Ishida, T. Nakajima, Y. Honda, O. Kitao, H. Nakai, T. Vreven, K. Throssell, J. A. Montgomery, Jr., J. E. Peralta, F. Ogliaro, M. J. Bearpark, J. J. Heyd, E. N. Brothers, K. N. Kudin, V. N. Staroverov, T. A. Keith, R. Kobayashi, J. Normand, K. Raghavachari, A. P. Rendell, J. C. Burant, S. S. Iyengar, J. Tomasi, M. Cossi, J. M. Millam, M. Klene, C. Adamo, R. Cammi, J. W. Ochterski, R. L. Martin, K. Morokuma, O. Farkas, J. B. Foresman and D. J. Fox, *Gaussian 16*, Gaussian, Inc., Wallingford CT, 2016.

81 F. Weigend and R. Ahlrichs, Balanced basis sets of split valence, triple zeta valence and quadruple zeta valence quality for H to Rn: Design and assessment of accuracy, *Phys. Chem. Chem. Phys.*, 2005, **7**, 3297–3305.

82 J. Tomasi, B. Mennucci and R. Cammi, Quantum mechanical continuum solvation models, *Chem. Rev.*, 2005, **105**, 2999–3094.

83 F. Neese, The ORCA program system, *Wiley Interdiscip. Rev.: Comput. Mol. Sci.*, 2012, **2**, 73–78.

84 F. Neese, Software update: the ORCA program system, version 4.0, *Wiley Interdiscip. Rev.: Comput. Mol. Sci.*, 2018, **8**, e1327.

85 C. Angeli, R. Cimiraglia, S. Evangelisti, T. Leininger and J.-P. Malrieu, Introduction of  $n$ -electron valence states for multireference perturbation theory, *J. Chem. Phys.*, 2001, **114**, 10252–10264.

86 P.-Å. Malmqvist and B. O. Roos, The CASSCF state interaction method, *Chem. Phys. Lett.*, 1989, **155**, 189–194.

87 S. Kossmann and F. Neese, Comparison of two efficient approximate Hartree–Fock approaches, *Chem. Phys. Lett.*, 2009, **481**, 240–243.

88 F. Weigend, Hartree–Fock exchange fitting basis sets for H to Rn, *J. Comput. Chem.*, 2008, **29**, 167–175.

89 B. A. Heß, C. M. Marian, U. Wahlgren and O. Gropen, A mean-field spin-orbit method applicable to correlated wavefunctions, *Chem. Phys. Lett.*, 1996, **251**, 365–371.

90 C. Riplinger and F. Neese, An efficient and near linear scaling pair natural orbital based local coupled cluster method, *J. Chem. Phys.*, 2013, **138**, 034106.

91 C. Riplinger, P. Pinski, U. Becker, E. F. Valeev and F. Neese, Sparse maps—A systematic infrastructure for reduced-scaling electronic structure methods. II. Linear scaling domain based pair natural orbital coupled cluster theory, *J. Chem. Phys.*, 2016, **144**, 024109.

92 A. V. Marenich, C. J. Cramer and D. G. Truhlar, Universal Solvation Model Based on Solute Electron Density and on a Continuum Model of the Solvent Defined by the Bulk Dielectric Constant and Atomic Surface Tensions, *J. Phys. Chem. B*, 2009, **113**, 6378–6396.

